J. Mech. Phys. Solids 196 (2025) 105999

Contents lists available at ScienceDirect

Journal of the Mechanics and Physics of Solids

journal homepage: www.elsevier.com/locate/jmps

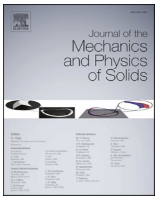

Biomimetic Turing machine: A multiscale theoretical framework for the inverse design of target space curves

JiaHao Li [a,1], Xiaohao Sun [a,1], ZeZhou He [a], YuanZhen Hou [a], HengAn Wu [a,b,*], YinBo Zhu [a,*]

[a] *CAS Key Laboratory of Mechanical Behavior and Design of Materials, Department of Modern Mechanics, University of Science and Technology of China, Hefei 230027, China*
[b] *State Key Laboratory of Nonlinear Mechanics, Institute of Mechanics, Chinese Academy of Science, 15 Beisihuan West Road, Beijing 100190, China*

ARTICLE INFO

Keywords:
Morphing materials
Space curves
Programmable ribbon
Inverse design
Microstructure encoding

ABSTRACT

Morphing ribbons and their inverse design are usually confined to plane curves, since in most cases only the curvature is considered. Given that curvature and torsion are equally important geometric characteristics of space curves, it is urgent to propose a systematic theoretical framework for the inverse design. Toward this end, we here present a multiscale theoretical framework named biomimetic Turing machine (BTM) to achieve desired target space curves, which is inspired from two microstructural regulation mechanisms behind the hydration-driven morphing of plant tissues: the graded curvature regulated by matrix volume fraction (c_m) and the helix-like morphology regulated by fibril orientation angle (FOA). By analogizing to Turing machine encoded by binary mapping, the proposed BTM can inversely encode a morphing ribbon with preset microstructural parameters (FOA and c_m) to achieve desired target space curves. The proposed theoretical framework can first bridge the microstructural fiber-matrix swelling and the macroscopic ribbon morphing as a forward problem, in which a twist field is subsequently introduced to create the kinematic map between the target space curve and the ribbon, innovatively posing the inverse design as an initial value problem. To facilitate the experimental implementation of BTM, we further propose an optimization strategy for selecting the twist field and provide design criteria as guidelines for experiments. As a conceptual display, we present a phase diagram in the c_m versus FOA plane to illustrate the complex target morphologies (e.g., hemisphere, hyperboloid, and tendril) characterized by various parameters of curvature and torsion designed rationally by the BTM theory, while in previous studies the morphing morphologies (e.g., helices, arcs, and helicoid ribbons) exhibit only constant curvature or torsion. This work presents a novel inverse design strategy for space curves with both curvature and torsion, broadening the potential for the design and fabrication of morphing materials.

1. Introduction

Programmable materials have garnered significant attention in recent years due to their controllable mechanical, optical, acoustic,

---

[*] Corresponding authors.
E-mail addresses: wuha@ustc.edu.cn (H. Wu), zhuyinbo@ustc.edu.cn (Y. Zhu).
[1] These authors contributed equally to this paper.

https://doi.org/10.1016/j.jmps.2024.105999
Received 19 August 2024; Received in revised form 26 November 2024; Accepted 2 December 2024
Available online 6 December 2024
0022-5096/© 2024 Elsevier Ltd. All rights are reserved, including those for text and data mining, AI training, and similar technologies.

morphological, and other physical properties. Among these, morphing materials are the most widely concerned, as they can alter the geometrical shape in response to external stimuli. Due to their exceptional deformation controllability, morphing materials have found extensive applications in various engineering fields, including wearable electronics (Shen et al., 2024), biomedical devices, robotics (Ha et al., 2020; Shin et al., 2018), food processing (Tao et al., 2021), the aerospace industry (Zhang et al., 2022), and agriculture (Luo et al., 2023).

Realizing the morphology design of morphing material draws great concern both theoretically and experimentally during past two decades. As a pioneering work, Sharon et al. developed the theoretical framework of non-Euclidean elastic plates (Armon et al., 2011; Efrati et al., 2009; Klein et al., 2007), in which an intermediate configuration is introduced to describe the stress-free state. The non-Euclidean elastic plate theory suggests that the stretch energy of a non-Euclidean elastic plate can be represented as the Poisson's ratio-weighted Lˆ2 norm of the first fundamental form of the surface between the target and intermediate configurations. Similarly, the bending energy can be represented as the Lˆ2 norm of the second fundamental form (Efrati et al., 2009; Pezzulla et al., 2017). The equivalence of energy form between non-Euclidean elastic plates and bilayer plates is elucidated by (Van Rees et al., 2017). Building on this theory, the feasibility of morphing plate has been experimentally realized through the pneumatic and thermal actuation (Aharoni et al., 2018; Boley et al., 2019; Siéfert et al., 2019). This technology even allows for the morphing of complex target shapes, such as human faces and flowers (Sydney Gladman et al., 2016).

Although considerable effort efforts have been made on the rational design of morphing materials, there are two issues remain unresolved. Firstly, due to the geometry restriction by 2D structures of morphing plate, realizing the inverse design of the complex target shape from plate is still a challenging problem. For example, if we want to morph a target shape with large Gaussian curvature

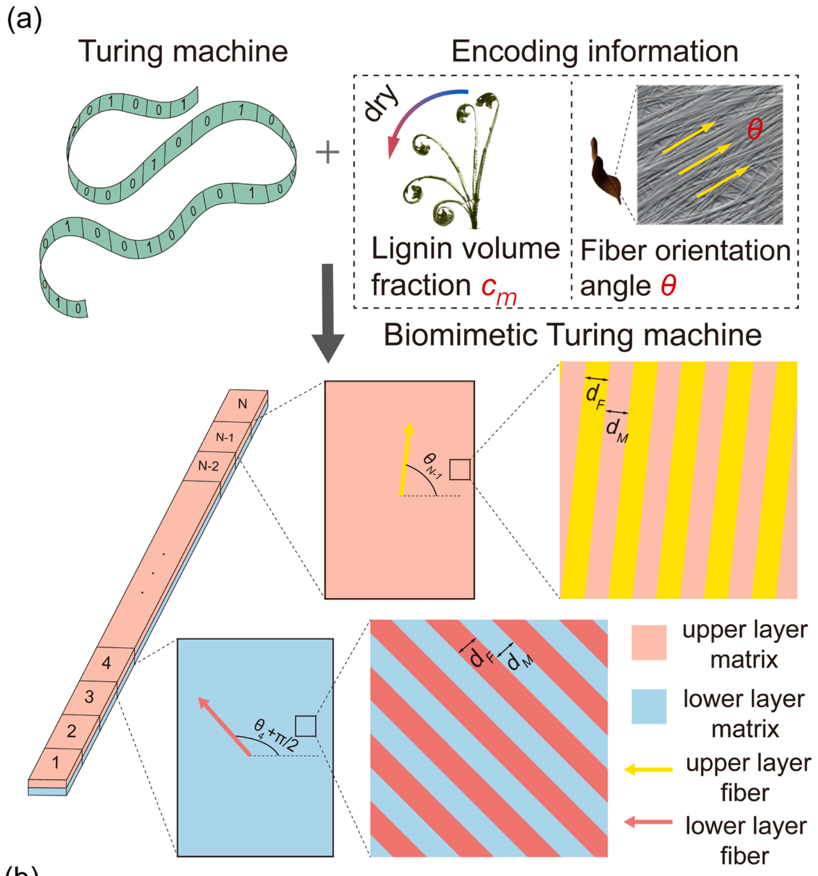

(b)

	Input	Rule	Output
Original Turing machine	Information (0,1)	Math operation	Information (0,1)
Biomimetic Turing machine	Humidity	Microstructures	Morphology

Fig. 1. Basic concept of the BTM. (a) Schematic illustration of the BTM encoded by the volume fraction and the fiber orientation angle inspired from hydration actuated movements of plant tissues: non-uniform distribution of lignin volume fraction in *Selaginella lepidophylla* (Rafsanjani et al., 2015) reproduced with permission, Copyright 2015, Springer Nature Publications and fiber orientation angle in plant cell wall (Cosgrove, 2024) reproduced with permission, Copyright 2024, Springer Nature Publications. (b) The analogy of input, rule and output between Turing machine and BTM.

such as sphere from a plate, significant in-plane stretching is required according to *Theorema Egregium* (Pezzulla et al., 2016; Siéfert et al., 2019). Unfortunately, Timoshenko's formula only holds for small mismatched strain and large residual strain causes complicated nonlinear relationship between curvature, external stimuli and geometric sizes (Liu et al., 2023, 2019; Timoshenko, 1925). Secondly, to the best of our knowledge, the morphologies of morphing ribbons in previous studies are confined to two categories: the plane curves, where only curvature is considered, and helices or helicoids with constant curvature and torsion (Sun et al., 2024, 2022). The inverse design of target space curves framed by both curvature and torsion has not been adequately investigated. Therefore, the question arises: can we manipulate the microstructures of a morphing ribbon to attain a targeted space curve with both curvature and torsion, thereby achieving the inverse design of curve-discretized surfaces with significant Gaussian curvature?

Nature shows us the answer. The movement of hydration actuated plant tissues brought about widespread attention during past three decades (Quan et al., 2020). Although morphologies of hydration actuated plant tissues are different in colorful ways, the mechanisms of hydration actuation patterns can be classified into two types. The first one is the gradient curvature of bilayer structures caused by the non-uniform volume fraction (c_m) of amorphous matter (e.g., lignin and hemicellulose) known as gradient lignification. This has been observed in *Selaginella lepidophylla*, pine cones, and other plant species (Rafsanjani et al., 2015; Reyssat and Mahadevan, 2009; F. Zhang et al., 2022). These curvature gradient structures give rise to hydration actuated curling plane curve morphologies, such as arcs in pine cones and spirals in *Selaginella lepidophylla* (Fig. 1(a)). However, hydration actuated movement not only occurs in a plane but also in spatial dimension. Fiber orientation angle (FOA), as the second one, restricts the deformation direction to generate helix curve. Examples include the helix in dehydrated leaves (Fig. 1(a)) and the helicoid in chiral seed pods, *Dendrobium helix*, and *Prosthechea cochleata* (Armon et al., 2011; Huang et al., 2018). The arc, spiral, helicoid, and helix mentioned before are common morphologies in plants, but when we combine these two mechanisms together, we can transcend the existing structures in nature and create the more complex morphologies artificially. In 1936, Alan Turing introduced an abstract model, referred to as Turing machine, which is capable of manipulating symbols on a ribbon based on a set of predetermined rules (Turing, 1937). This model serves as a fundamental theoretical framework for the implementation of various computer algorithms. In classical information theory, symbols in Turing machine are typically represented using two distinct states, usually designated as 0 and 1. However, if we extend this concept and consider information as the two microstructures inspired from hydration actuated plant tissues in nature, it opens up a myriad of fascinating possibilities.

Inspired by the hydration actuation patterns in nature and Turing machine, we develop a multiscale theoretical framework, biomimetic Turing machine (BTM), to encode the microstructures (c_m and FOA) of a morphing ribbon for the inverse design of a target space curve with both curvature and torsion. Furthermore, based on the BTM theory we inversely design the curved surface with positive and negative Gaussian curvatures discretized by space curve as well as tendril in nature successfully. This paper is organized as follows. In Section 2, we present the forward problem and solve it by building a multiscale model, consisting of three components. Firstly, we build the swelling constitutive for fiber-matrix composites in Section 2.2.1. Secondly, in Section 2.2.2, the relationship between principal curvatures of ribbon and swelling strain is derived by minimizing the elastic energy. By transforming the material frame to geometry frame, we derive the ribbon morphology with c_m and FOA as encoding information in Section 2.2.3. Then a strategy for inverse design is proposed in Section 3, consisting of introducing twist field in Section 3.1, the optimization strategy of twist field in Section 3.2 and the design criteria of geometry size in Section 3.3. As verifications, examples are given in Section 4. To compare with the previous works, we condense the BTM and the previous inverse design strategies for morphing ribbon into a phase diagram in Section 5. The perspective and potential applications of BTM are also discussed in this section. Eventually, we conclude this work in Section 6.

2. Forward problem and the multiscale model

2.1. Definition of the forward problem

We first define the forward problem. The structure of BTM, as depicted in Fig. 1(a), is a ribbon consisting of bilayer structure comprising upper layer and lower layer. Each layer is subdivided into several equally spaced units, which are composed of matrix (amorphous matter) and fibers. The widths of fibers and matrix are denoted as d_F and d_M, respectively, and the matrix volume fraction is defined as $c_m = d_M/(d_F+d_M)$. The fiber orientations in the upper layer and lower layer are perpendicular to each other. When external stimuli applied, the matrix swells perpendicular to the directions (characterized by FOA) of fibers. Accordingly, the center line of ribbon morphs to the target space curve by strain mismatch. The morphing process of BTM is similar to the encoding of Turing machine as shown in Fig. 1(b). In contrast to the binary information of Turing machine, the input and output of BTM are external stimuli and morphology, respectively. Similar to Turing machine, the central aspect of BTM lies on the rules governing the microstructures of the ribbon. Therefore, the forward problem is defined as follows: given the volume fraction and FOA of each unit, determine the curvature and torsion of the space curve. Correspondingly, the inverse design is to determine the volume fraction and FOA of each unit according to target space curve.

2.2. A multiscale model for the forward problem

We build the multiscale theoretical framework to solve the forward problem at first. In order to have a general understanding of the geometric structure, the basic unit and morphing process of BTM are shown in Fig. 2. The geometry parameters of each unit are defined as follows: length of each unit is l_0, the width is w and the thickness is $t/2$. As stated before, each unit is encoded by matrix volume fraction and FOA. Because the fiber orientation in upper layer and lower layer are perpendicular, we define the FOA of upper layer as θ

to represent the local FOA of bilayer. To describe the geometry of BTM clearly during morphing process, three frames are defined. The global frame, which consists of three axis {$\boldsymbol{i}, \boldsymbol{j}, \boldsymbol{k}$}, is fixed on the left end of the ribbon and represents the perspective of observer. The axis $\boldsymbol{i}, \boldsymbol{j}$ are along the width and length directions of the ribbon before morphing and the $\boldsymbol{k} = \boldsymbol{i} \times \boldsymbol{j}$ is perpendicular to the ribbon surface. The material frame {$\boldsymbol{d_1}, \boldsymbol{d_2}, \boldsymbol{N}$}, which describes intrinsic material properties, is attached to ribbon locally. $\boldsymbol{d_2}$ and $\boldsymbol{d_1}$ are along the longitudinal and transverse directions of fibers respectively and the normal vector $\boldsymbol{N}$ is defined as $\boldsymbol{d_1} \times \boldsymbol{d_2}$. The geometry frame, kinematic equations of which describe the geometry properties of BTM after morphing, is composed of {$\boldsymbol{E_1}, \boldsymbol{E_2}, \boldsymbol{N}$}. $\boldsymbol{E_2}$ and $\boldsymbol{E_1}$ are along the length and width directions of each unit respectively. Because {$\boldsymbol{d_1}, \boldsymbol{d_2}$} and {$\boldsymbol{E_1}, \boldsymbol{E_2}$} are in the same plane, the normal vector of upper layer can also be expressed as $\boldsymbol{N} = \boldsymbol{E_1} \times \boldsymbol{E_2}$. Note that the global frame is fixed but the geometry frame changes during morphing, so the material frame can be viewed as rotating the geometry frame counterclockwise along the $\boldsymbol{N}$ axis with θ.

2.2.1. Swelling constitutive

To elucidate the relationship between material properties and swelling strains, we begin by constructing a micro-mechanical swelling constitutive model in fiber-matrix structures. The swelling process observed in fiber-matrix composites bears resemblance to the swelling of plant cells. In plant tissues, cellulose nanofibers primarily contribute to the stiffness of cell wall and are immersed within an amorphous matrix comprising hemicellulose and lignin (Cosgrove, 2024; Salmen, 2022, 2015; Zhang et al., 2021). Due to the crystalline structure, cellulose nanofibers are not susceptible to actuation by hydration (Hou et al., 2021; Xiao et al., 2024). However, they play a crucial role in transfer shear stress across the fiber-matrix interface due to high stiffness, which restricts the swelling direction. Consequently, the swelling strain along $\boldsymbol{d_1}$ direction tends to be much larger than $\boldsymbol{d_2}$ direction. To quantitatively characterize the swelling process, we develop a swelling constitutive model from the bottom to up. Here, we specify that for simplicity, only the long fiber model is selected, while the swelling constitutive of other types of fiber-matrix models is explored in Appendix B. Before building the micro-mechanical model of swelling, some assumptions regarding fibers and matrix are listed as follows: (i) The mechanical properties of matrix and fibers are isotropic. (ii) The Poisson's ratio of fibers is too small to be considered. (iii) Only matrix swells but fibers cannot. (iv) The swelling strain of matrix η is too small to affect the Young's modulus. (v) There is no slip on the fiber-matrix interface.

We consider the micro-mechanical swelling constitutive model in material frame as illustrated in Fig. 3(a). Considering the periodic arrangement of the fiber-matrix structure, representative volume element (RVE) is selected. When the RVE swells, the shear stress on fiber-matrix interface tends to compress matrix and stretch fibers along $\boldsymbol{d_2}$ direction (Fig. 3(a)). The constitutive of fiber in $\boldsymbol{d_1}$ and $\boldsymbol{d_2}$ directions can be expressed as:

$$\begin{cases} \sigma_{F1} = E_F \varepsilon_{F1} \\ \sigma_{F2} = E_F \varepsilon_{F2} \end{cases}, \tag{1}$$

where σ_{F1} and σ_{F2} are stresses of fibers along $\boldsymbol{d_1}$ and $\boldsymbol{d_2}$ directions, respectively and the strains of the fibers are ε_{F1} and ε_{F2}. Considering the assumptions (i) and (ii), only one elastic constant is needed and the Young's modulus of fibers is defined as E_F. Based on assumptions (iii), the matrix has isotropic swelling strain, so we assume the swelling strain of matrix along $\boldsymbol{d_1}$ and $\boldsymbol{d_2}$ directions is η. Considering the swelling strain is small (assumptions (iv)) as well as using the multiplicative decomposition of strain gradient (Colorado-Cervantes et al., 2022; Yavari, 2010), we get the constitutive of the matrix:

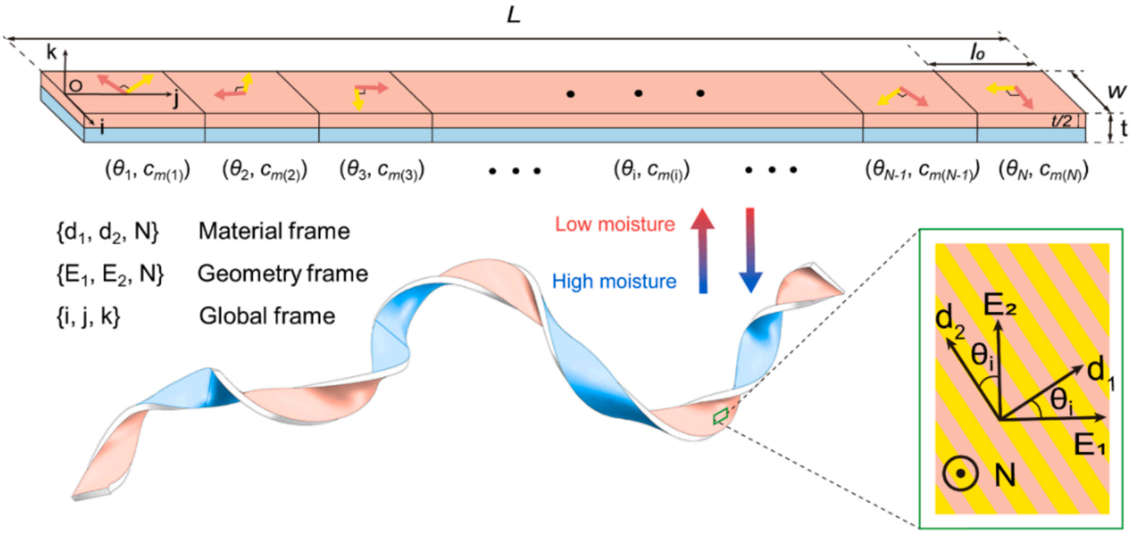

Fig. 2. Schematic illustration of morphing process of BTM. The BTM is divided into N units and each unit is encoded by θ and c_m. BTM morphs to the target space curves after being actuated. Material frame is along the longitudinal and transverse direction of fiber in each unit and the geometry frame is attach to each unit.

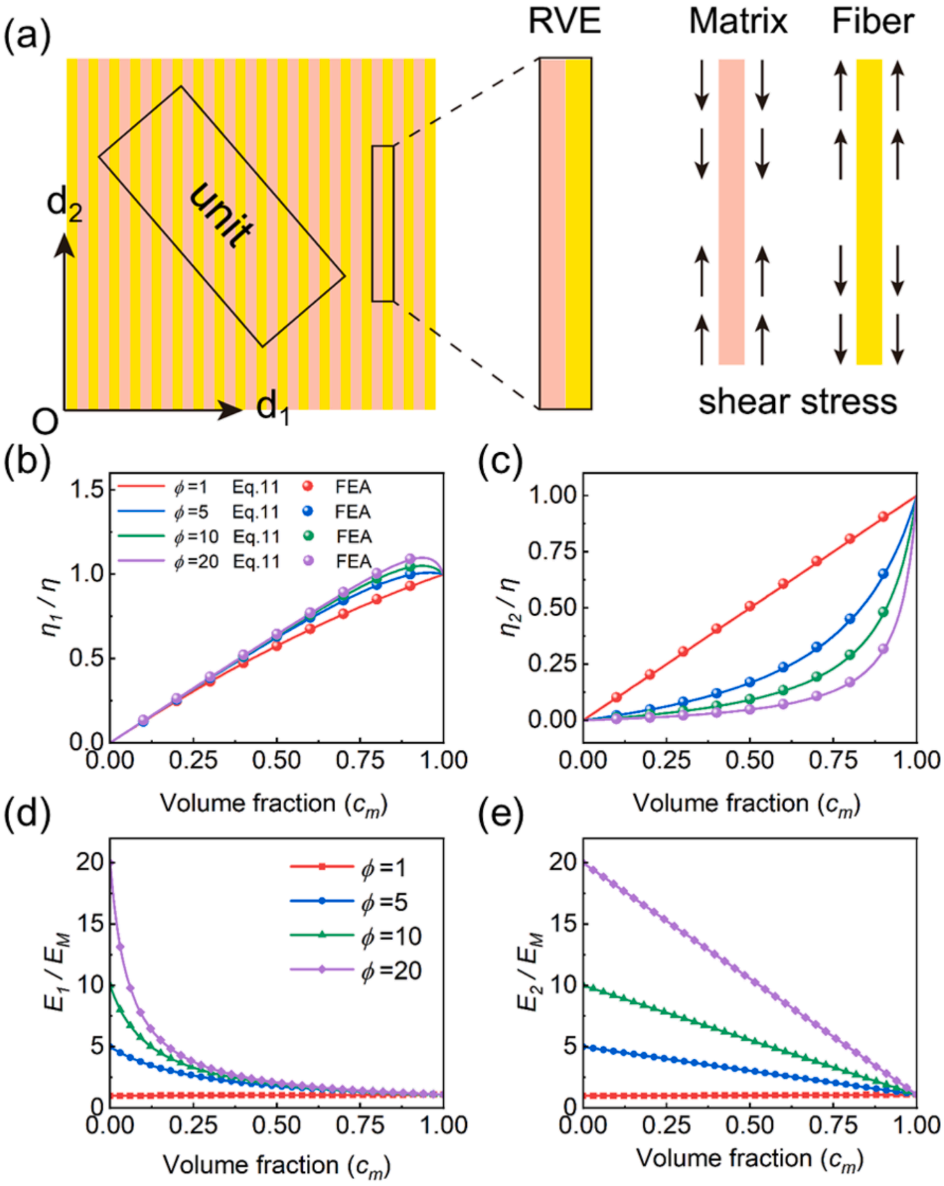

Fig. 3. The constitutive of upper layer unit in material frame. (a) Schematic illustration of representative volume element (RVE) composed of fiber and matrix. (b) (c) Swelling strain ratio of RVE and matrix as a function of matrix volume fraction under different fiber-matrix stiffness ratios in $\boldsymbol{d_1}$ and $\boldsymbol{d_2}$ axis respectively. (d-e) Elastic modulus of RVE and matrix as functions of matrix volume fraction under different fiber-matrix stiffness ratios in $\boldsymbol{d_1}$ and $\boldsymbol{d_2}$ axis respectively.

$$\begin{cases} \sigma_{M1} = \dfrac{E_M}{1-\nu^2}(\varepsilon_{M1}-\eta) + \dfrac{\nu E_M}{1-\nu^2}(\varepsilon_{M2}-\eta) \\ \sigma_{M2} = \dfrac{\nu E_M}{1-\nu^2}(\varepsilon_{M1}-\eta) + \dfrac{E_M}{1-\nu^2}(\varepsilon_{M2}-\eta) \end{cases}, \tag{2}$$

where σ_{M1} and σ_{M2} are the stresses of matrix along the $\boldsymbol{d_1}$ and $\boldsymbol{d_2}$ directions, respectively and the strains of the matrix are ε_{M1} and ε_{M2}. E_M is the Young's modulus of matrix and ν is the Poisson's ratio. Then we consider the shear stress transfer on the interface and applied the assumption (v)). Then the stress and strain relationship between matrix and fibers can be expressed as:

$$\begin{cases} \sigma_2 = c_m\sigma_{M2} + (1-c_m)\sigma_{F2}, \sigma_1 = \sigma_{F1} = \sigma_{M1} \\ \varepsilon_1 = c_m\varepsilon_{M1} + (1-c_m)\varepsilon_{F1}, \varepsilon_2 = \varepsilon_{M2} = \varepsilon_{M2} \end{cases}, \tag{3}$$

where the strains and stresses of the RVE along $\boldsymbol{d_1}$ and $\boldsymbol{d_2}$ directions are ε_1, ε_2 and σ_1, σ_2 respectively. Combining Eqs. (1), (2) and (3), we can solve the swelling stress of RVE:

$$\begin{cases} \sigma_1 = \dfrac{E_F(c_m(-\eta(\nu+1)+\nu\varepsilon_2)+\varepsilon_1)}{(1-\nu^2)\phi c_m+(1-c_m)} \\ \sigma_2 = \dfrac{E_M\left(\left(c_m^2(\phi(\nu+1)-1)((\nu-1)\varepsilon_2\phi+\varepsilon_2-\eta)\right)+c_m\left(\nu\varepsilon_1\phi+\varepsilon_2\left((\phi-1)^2-\nu^2\phi^2\right)\right)-\eta\right)}{c_m(1-\nu^2)\phi+(1-c_m)} \end{cases}, \tag{4}$$

where $\phi = E_F/E_M$ is the modulus ratio of fibers and matrix. When there is no external stress applied, the RVE will be relaxed to a stress-free configuration. To solve the swelling strain of stress-free configuration, we set the stresses of RVE equal zero and finally we get:

$$\begin{cases} \eta_1 = \dfrac{c_m+(\nu+1)\phi(1-c_m)}{c_m+(1-c_m)\phi}c_m\eta \\ \eta_2 = \dfrac{1}{c_m+(1-c_m)\phi}c_m\eta \end{cases}, \tag{5}$$

η_1, η_2 are the effective swelling strain of the RVE in material frame. Note that the constitutive of RVE can be expressed as:

$$\begin{pmatrix} \sigma_1 \\ \sigma_2 \end{pmatrix} = \mathbf{D}\begin{pmatrix} \varepsilon_1 \\ \varepsilon_2 \end{pmatrix}, \tag{6}$$

where $\boldsymbol{D}$ is the stiffness matrix of RVE. Comparing Eqs. (4) and (6), the stiffness matrix of RVE can be derived:

$$\mathbf{D} = \begin{pmatrix} 1 & \nu_0 \\ \nu_0 & 1+\delta \end{pmatrix}E, \tag{7}$$

where δ is a bias factor, representing the anisotropic properties of RVE. The bias factor, effective Poisson's ratio ν_0 and the effective Young's modulus E of RVE in Eq. (7) can be expressed as:

$$\begin{cases} \delta = (1-c_m)c_m(\phi(1-\nu)-1)(\phi(1+\nu)-1)/\phi \\ E = \dfrac{E_M\phi}{c_m(\phi(1-\nu^2)-1)+1} \\ \nu_0 = c_m\nu \end{cases}. \tag{8}$$

To elucidate the impact of volume fraction and stiffness ratio on swelling strains and Young's modulus in the RVE along $\boldsymbol{d}_1$ and $\boldsymbol{d}_2$ directions, we set $\nu = 0.3$ and depict Eqs. (5) and (7) in Fig. 3(b-e). As the matrix volume fraction increases, the swelling composite expands, resulting in a corresponding increase in swelling strains in both directions of the RVE. When the stiffness ratio equals 1, it implies that the mechanical properties of the matrix and fiber are nearly identical, except for the Poisson's ratio (which has a negligible impact). As a result, relationship between swelling strains and matrix volume fractions is nearly linear. Typically, due to the crystalline structure of fiber, its Young's modulus is typically much higher than matrix. For instance, the modulus ratio of cellulose nanofibers (90–120 GPa) and amorphous matrix (6–8 GPa) in plant cell wall is 10–20. Fig. 3(b-c) demonstrates that as the stiffness ratio increases, the swelling strain in the $\boldsymbol{d}_1$ direction increases, while decreasing in $\boldsymbol{d}_2$ direction. This is because the increased restriction in $\boldsymbol{d}_2$ direction of matrix, leading to a decrease of swelling strains. The increase of swelling strains with stiffness ratio increasing in $\boldsymbol{d}_1$ direction is attributed to the Poisson's effect, resulting from the decrease of swelling strains in $\boldsymbol{d}_2$ direction. If there is no Poisson's effect, Eq. (5) reduces to $\eta_1/\eta = c_m$, which is independent of the stiffness ratio ϕ. Fig. 3(d-e) suggest that the Young's modulus decreases with increasing matrix volume fraction, while it increases with the stiffness ratio.

Now, we have established the swelling constitutive of upper layer, as the fiber orientation is perpendicular in both upper layer and lower layer. Hence the constitutive of lower layer can be derived similarly. However, how the constitutive of RVE determines the principal curvatures of unit remains unclear and will be addressed in next section.

2.2.2. Principal curvatures

Strain mismatch is a fundamental principle underlying the deformation of bilayers since the early 20th century (Timoshenko, 1925). In the context of BTM, the perpendicular fiber orientation of upper layer and lower layer leads to an orthorhombic swelling. Consequently, the strain mismatches in two orthogonal directions are independent. In this section, we construct a model to illustrate how swelling affects the principal curvatures of unit by strain mismatch.

We consider this process within material frame. Since the axis of the material frame aligns along the swelling directions, there is no shear strain for both the upper and lower layers. Therefore the energy per unit area, without considering shearing in the material frame, can be expressed as:

$$U = \frac{1}{2}\int_0^{t/2}(\boldsymbol{\varepsilon}_a-\boldsymbol{\eta}_a)^t\mathbf{D}_a(\boldsymbol{\varepsilon}_a-\boldsymbol{\eta}_a)dz + \frac{1}{2}\int_{-t/2}^{0}(\boldsymbol{\varepsilon}_b-\boldsymbol{\eta}_b)^t\mathbf{D}_b(\boldsymbol{\varepsilon}_b-\boldsymbol{\eta}_b)dz, \tag{9}$$

where $\boldsymbol{\varepsilon}_a$, $\boldsymbol{\varepsilon}_b$ are the elastic strain, $\boldsymbol{\eta}_a$, $\boldsymbol{\eta}_b$ are the effective swelling strains vectors, $\boldsymbol{D}_a$, $\boldsymbol{D}_b$ are the stiffness matrix for upper and lower layers, z is the coordination along $\boldsymbol{N}$. Using the Kirchhoff-Love hypothesis, the elastic strain is expressed as:

$$\boldsymbol{\varepsilon}_a = \boldsymbol{\varepsilon}_{\mathrm{b}} = \begin{pmatrix} \varepsilon_1 \\ \varepsilon_2 \end{pmatrix} + z \begin{pmatrix} \kappa_1 \\ \kappa_2 \end{pmatrix}. \tag{10}$$

Considering the fiber orientations are perpendicular in upper and down layers, the swelling strains and stiffness matrix can be expressed as:

$$\begin{cases} \boldsymbol{\eta}_a = \begin{pmatrix} \eta_1 \\ \eta_2 \end{pmatrix}, \boldsymbol{\eta}_b = \begin{pmatrix} \eta_2 \\ \eta_1 \end{pmatrix} \\ \mathbf{D}_a = \begin{pmatrix} 1 & \nu_0 \\ \nu_0 & 1+\delta \end{pmatrix} E, \mathbf{D}_b = \begin{pmatrix} 1+\delta & \nu_0 \\ \nu_0 & 1 \end{pmatrix} E \end{cases}, \tag{11}$$

simplify Eq. (9), we get:

$$\begin{aligned} U = {} & \frac{t^3 E}{24}\left(\left(1-\nu+\frac{\delta}{2}\right)\mathrm{tr}\left(\boldsymbol{\kappa}^2\right)+\nu\mathrm{tr}^2(\boldsymbol{\kappa})\right) \\ & + \frac{tE}{2}\left((1-\nu)\mathrm{tr}(\boldsymbol{\varepsilon}-\overline{\boldsymbol{\eta}})^2+\nu\mathrm{tr}^2(\boldsymbol{\varepsilon}-\overline{\boldsymbol{\eta}})+\frac{(1-\nu)}{2}(\eta_2-\eta_1)^2+\left((\varepsilon_2-\eta_2)^2+(\varepsilon_1-\eta_2)^2\right)\frac{\delta}{2}\right), \\ & + \frac{t^2 E}{8}\left((\eta_2-\eta_1)(\kappa_1-\kappa_2)(1-\nu)+((\varepsilon_2-\eta_2)\kappa_2-(\varepsilon_1-\eta_2)\kappa_1)\delta\right) \end{aligned} \tag{12}$$

where tr(·) donates the trace of a second-order tensor, $\boldsymbol{\kappa}$ is the curvature tensor, $\boldsymbol{\varepsilon}$ is the real strain and $\overline{\boldsymbol{\eta}}$ is the mean swelling tensor.

$$\begin{cases} \boldsymbol{\kappa} = \begin{pmatrix} \kappa_1 & 0 \\ 0 & \kappa_2 \end{pmatrix} \\ \boldsymbol{\varepsilon} = \begin{pmatrix} \varepsilon_1 & 0 \\ 0 & \varepsilon_2 \end{pmatrix} \\ \overline{\boldsymbol{\eta}} = \begin{pmatrix} \frac{\eta_1+\eta_2}{2} & 0 \\ 0 & \frac{\eta_1+\eta_2}{2} \end{pmatrix} \end{cases} \tag{13}$$

It is obvious that if the swelling is isotropic and the mechanical properties is isotropic by setting $\delta = 0$ and $\eta_0 = \eta_1 = \eta_2$, we can get a degenerated energy form similar to the non-Euclidean plate proposed by (Armon et al., 2011; Klein et al., 2007).

$$U = \frac{Et^3}{24}\left((1-\nu)\mathrm{tr}\left(\boldsymbol{\kappa}^2\right)+\nu\mathrm{tr}^2(\boldsymbol{\kappa})\right)+\frac{Et}{2}\left((1-\nu)\mathrm{tr}(\boldsymbol{\varepsilon}-\overline{\boldsymbol{\eta}})^2+\nu\mathrm{tr}^2(\boldsymbol{\varepsilon}-\overline{\boldsymbol{\eta}})\right) \tag{14}$$

We minimize the energy per unit area by setting the variation of Eq. (12) equal zero:

$$\frac{\delta U}{\delta \varepsilon_1} = \frac{\delta U}{\delta \varepsilon_2} = 0; \frac{\delta U}{\delta \kappa_1} = \frac{\delta U}{\delta \kappa_2} = 0. \tag{15}$$

Finally, we get the strain and principal curvatures:

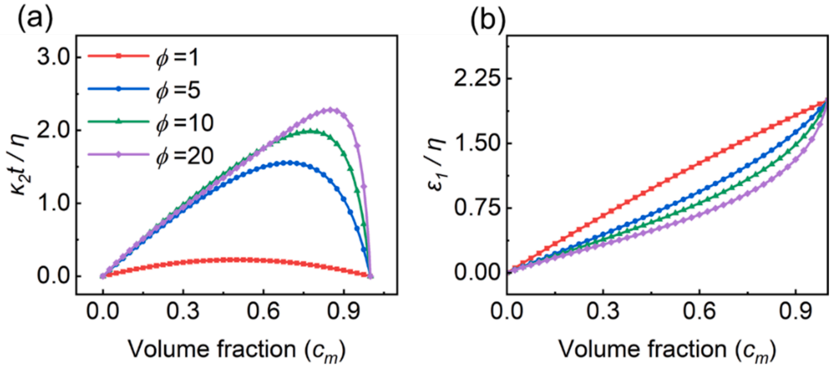

Fig. 4. Dimensionless principal curvature (a) and strain (b) as functions of matrix volume fraction under different fiber-matrix stiffness ratios.

$$\varepsilon_1 = \varepsilon_2 = \frac{2c_m\eta\left(\delta^2 + 8 - 8c_m^2\nu^2 + \delta(9 - c_m\nu) + (c_m + \phi(1 - c_m)(1 + \nu))\left(8\left(1 - c_m^2\nu^2\right) + \delta(c_m\nu + 7)\right)\right)}{\left(\delta^2 + 16\left(1 + \delta - c_m^2\nu^2\right)\right)(c_m + \phi(1 - c_m))}, \tag{16}$$

$$\kappa_2 = -\kappa_1 = \frac{48(1 - c_m)\left(1 + \delta - c_m^2\nu^2\right)(\phi(\nu + 1) - 1)c_m\eta}{t\left(\delta^2 + 16\left(1 + \delta - c_m^2\nu^2\right)\right)(c_m + \phi(1 - c_m))}, \tag{17}$$

when $\phi = 1, \nu = 0, c_m = 0.5, \delta = 0$, Eq. (17) degenerates to the classical equation of curvature of bi-mental ($\kappa = 3\eta/2t$) given by (Timoshenko, 1925).

To elucidate the impact of the stiffness ratio and volume fraction on curvature and strain, we depict the dimensionless principal curvature $\kappa t/\eta$ and dimensionless strain ε/η in Fig. 4(a-b). When the volume fraction of the matrix is zero, it implies no swelling, thus both the principal curvature and strain are zero. As the matrix volume fraction increases, the $\kappa t/\eta$ initially rises, then declines to zero. This phenomenon is attributable to the fact that when the matrix volume fraction is minimal, increase in matrix volume fraction leads to increasing of swelling strain, thus augmenting the principal curvature. Nonetheless, as the volume fraction trend approaches unity, the orthogonal anisotropy of the composite gradually diminishes. This results in the swelling strain no longer being constrained orthogonally, thereby causing a decline of $\kappa t/\eta$ to zero. When the stiffness ratio increases, the restraining effect of the fiber is enhanced. Consequently, $\kappa t/\eta$ tends to increase and the strain diminishes. Note that $\kappa t/\eta$ is determined by the volume fraction uniquely according to the curve preceding the maximum point as depicted in Fig. 4(a). Therefore, we can solve the volume fraction inversely with the principal curvatures of the ribbon for the target space curve.

We have established a correlation between volume fraction and principal curvatures within material frame. Nevertheless, to solve the forward problem, θ, which determines the directions of principal curvatures, is also needed to be considered. We will determine the curvature and torsion of center line of BTM according to c_m and θ of each unit in subsequent section.

2.2.3. *Morphology of BTM*

To derive the morphology of BTM, we start to consider the center line in material frame, the motion equation of the material frame along the center line can be written as (Chen et al., 2011):

$$\mathbf{d}' = \mathbf{\Gamma}(\theta)\mathbf{d}$$
$$\mathbf{\Gamma}(\theta) = \begin{pmatrix} 0 & 0 & -\kappa_1\sin\theta \\ 0 & 0 & -\kappa_2\cos\theta \\ \kappa_1\sin\theta & \kappa_2\cos\theta & 0 \end{pmatrix}, \tag{18}$$

where $(\cdot)'$ donates $d(\cdot)/ds$, $\boldsymbol{d}$=$\{\boldsymbol{d_1}, \boldsymbol{d_2}, \boldsymbol{N}\}^t$ and $(\cdot)^t$ represents the transpose of vector or matrix. Note that the material frame can be derived by rotating the geometry frame counterclockwise with angle $\boldsymbol{\theta}$ along $\boldsymbol{N}$ as mentioned in Section 2:

$$\mathbf{d} = \mathbf{RE}$$
$$\mathbf{R} = \begin{pmatrix} \cos\theta & \sin\theta & 0 \\ -\sin\theta & \cos\theta & 0 \\ 0 & 0 & 1 \end{pmatrix}, \tag{19}$$

where $\boldsymbol{E}$=$\{\boldsymbol{E_1}, \boldsymbol{E_2}, \boldsymbol{N}\}^t$ .Combining Eqs. (18) and (19), we can derive the kinematic equation of geometry frame:

$$\mathbf{E}' = \boldsymbol{\Lambda}\mathbf{E}$$
$$\boldsymbol{\Lambda} = (\mathbf{R}_t' + \mathbf{R}^t\mathbf{\Gamma})\mathbf{R} = \begin{pmatrix} 0 & -\theta' & (\kappa_2 - \kappa_1)\sin\theta\cos\theta \\ \theta' & 0 & -\kappa_1\sin^2\theta - \kappa_2\cos^2\theta \\ (\kappa_1 - \kappa_2)\sin\theta\cos\theta & \kappa_1\sin^2\theta + \kappa_2\cos^2\theta & 0 \end{pmatrix}. \tag{20}$$

In consideration of Eq. (17), we set κ_1=-κ_2, then Eq. (20) is simplified as:

$$\boldsymbol{\Lambda} = \begin{pmatrix} 0 & -\theta' & -\kappa_1\sin2\theta \\ \theta' & 0 & \kappa_1\cos2\theta \\ \kappa_1\sin2\theta & -\kappa_1\cos2\theta & 0 \end{pmatrix}. \tag{21}$$

The tangent vector $\boldsymbol{E_2}$ can be expressed by the derivative of position $\mathbf{r}(s)$:

$$\mathbf{r}' = \mathbf{E}_2. \tag{22}$$

Note that the principal curvatures determined by c_m has been discussed formerly (Eq. (17), Fig. 4(a)), hence when c_m and θ are given as functions of arc length parameter s, Eqs. (20) and (21) as kinematic equations of the geometry frame can be solved directly and then the morphology of BTM can be derived by integrating Eq. (22). Eventually the forward problem is solved from bottom (c_m and θ) to up (morphology of BTM) with the multiscale model successfully.

To compare with the former studies, here a special case is considered. When we set θ as constant, Eq. (21) degenerates to:

$$\Lambda = \begin{pmatrix} 0 & 0 & -\kappa_1 \sin 2\theta \\ 0 & 0 & \kappa_1 \cos 2\theta \\ \kappa_1 \sin 2\theta & -\kappa_1 \cos 2\theta & 0 \end{pmatrix}. \tag{23}$$

Note that $\{\boldsymbol{E}_1, \boldsymbol{E}_2, \boldsymbol{N}\}$ are the binormal vector, tangent vector and normal vector, Eq. (23) describe a space curve, whose curvature $\kappa = \kappa_1 \cos 2\theta$ and torsion $\tau = \kappa_1 \sin 2\theta$. Here, we examine two straightforward examples: plane curve and helix, to which most of the actuator design reported in previous studies can be attributed (Chen et al., 2012; Ha et al., 2020; Kuang et al., 2019).

We consider θ is 0 or $\pi/2$ and κ_1 as function of arc length parameter s, the torsion is zero and curvature is $\pm\kappa_1$. Eq. (23) degenerates to Frenet frame of plane curve. This instance is commonly employed to morph the circumferentially discrete part of revolved surface (Cheng et al., 2023; Kansara et al., 2023; Yang et al., 2023a; Zhang, 2022). Note that for many materials, it is nearly impossible to realize the shrinkage and swelling at the same time, which means we cannot morph a plane curve with both positive and negative curvatures (Ha et al., 2020; Kuang et al., 2019). However, in BTM theory we can morph a plane curve with both positive and negative curvatures by adjusting θ equals to 0 or $\pi/2$ as demonstrated in clover example as follows.

Considering both θ and κ_1 are constants, the torsion divided by curvature is constant (Eq. (24)), which is the definition of general helix (Abbena et al., 2006).

$$\frac{\tau}{\kappa} = \tan 2\theta = const. \tag{24}$$

The pitch p, radius R and helix angle ψ are given by Eq. (25).

$$p = \frac{2\pi}{\kappa_1} \sin\psi, R = \frac{\cos\psi}{\kappa_1}, \psi = -2\theta \tag{25}$$

A special case is when κ is vanishing but τ is not, considering Eq. (24) $\tan 2\theta$ must be infinite. Therefore, when $\theta = \pi/4$, pitch is zero and the morphing shape is helicoid (Armon et al., 2011; Chen et al., 2011). The general helix case can be solved analytically, we assume the point on the ribbon $\boldsymbol{r}$ can be parameterized with $\{s, t\}$, t is the distance parameter along the short edge. We solve the center line of the ribbon at first with the boundary condition Eq. (26):

$$\mathbf{E}(0,0) = \{\mathbf{i}, \mathbf{j}, \mathbf{k}\}, \mathbf{r}(0,0) = 0. \tag{26}$$

Combining Eqs. (22), (23) and (26), we can solve the parametric equations of center line. The Frenet frame along the short edge direction of the ribbon can be written as:

$$\dot{\mathbf{r}}(s,t) = \mathbf{E}_1(s,t), \tag{27}$$

$$\dot{\mathbf{d}} = \boldsymbol{\Gamma}(\theta + \pi/2)\mathbf{d}, \tag{28}$$

where $(\dot{\ })$ donates $d(\cdot)/dt$. The solution of center line $\{\boldsymbol{r}(s,0), \boldsymbol{E}_1(s,0), \boldsymbol{E}_2(s,0), \boldsymbol{N}(s,0)\}$ can serve as the initial value of Eqs. (27) and (28). Finally, the general helix shape can be solved analytically as:

$$\mathbf{r}(s,t) = X(s,t)\mathbf{i} + Y(s,t)\mathbf{j} + Z(s,t)\mathbf{k}$$
$$\begin{cases} X(s,t) = s\sin\psi + \dfrac{t(\cos\psi - \cos 3\psi)}{2} + \dfrac{\sin\gamma t \cos\psi \cos 2\psi}{\gamma} \\ Y(s,t) = \dfrac{\cos\psi \sin\gamma s \cos\gamma t}{\gamma} - \dfrac{2\sin\psi \cos^2\psi \cos\gamma s \sin\gamma t}{\gamma} + t\sin\psi \cos 2\psi \cos\gamma s \\ Z(s,t) = \dfrac{\cos\psi(\cos\gamma s \cos\gamma t - 1)}{\gamma} + \dfrac{2\sin\psi \cos^2\psi \sin\gamma s \sin\gamma t}{\gamma} - t\sin\psi \cos 2\psi \sin\gamma s \end{cases}. \tag{29}$$

For general case, when θ and c_m are given as functions of s, we can derive the morphology of center line of BTM by solving Eqs. (17), (21) and (22). However, for a specific curve, there is still unclear to design the c_m and θ of each unit inversely. Therefore, in subsequent section we will post a method to design the c_m and θ of each unit inversely according to the target space curve as center line of BTM.

3. Inverse design

Shape inverse design is defined as morphing to a target shape under external stimuli by controlling the microstructure. To the best of our knowledge, although significant experimental and theoretical efforts have been made to design and fabricate numerous actuators, the morphing shapes of ribbon are restricted to three types (arc, helix, and helicoid) and realizing inverse design for complex target shape of space curve is still a challenge. We build a theory for inverse design as follows.

3.1. Inverse design by introducing a twist field

Before considering the target center line, we note that all elements in the upper triangle part of Eq. (21) for the geometry frame exhibit non-zero values. This is because BTM is a ribbon structure and an extra parameter is required to determine the normal direction

N. However, when we consider a target space curve framed by Frenet frame, a notable observation emerges: only two parameters (curvature and torsion) are needed to frame a curve. This means we cannot achieve the inverse design by equating the geometry frame of BTM and the Frenet frame of target space curve directly.

To solve this problem, we note that the application of a twist field along the tangent vector of the center line of a ribbon has no influence on the shape of center line. Instead, it merely alters the orientations of the normal vector and binormal vector, as illustrated in Fig. 5(a). In other words, there is no more way to frame a curve (Bishop, 1975). Consequently, for a target space curve, arbitrary twist field is available to be applied along the tangent vector. Drawing upon this principle, a twist field $\varphi(s)$ is introduced along the tangent vector of target curve, which is unknown to be solved. We assume the kinematic equation of Frenet frame of target curve is:

$$\frac{d}{ds}\begin{pmatrix}\mathbf{B}\\ \mathbf{T}\\ \mathbf{N}_0\end{pmatrix}=\begin{pmatrix}0 & 0 & -\tau\\ 0 & 0 & \kappa\\ \tau & -\kappa & 0\end{pmatrix}\begin{pmatrix}\mathbf{B}\\ \mathbf{T}\\ \mathbf{N}_0\end{pmatrix}, \tag{30}$$

where the ***T, N***$_0$ and ***B*** represent the tangent vector, normal vector, and binormal vector of target curve, respectively, while κ and τ denote the curvature and torsion. Introducing a twist field φ(s) along ***T***, the rotational relationship can be expressed as:

$$\begin{pmatrix}\mathbf{B}_1\\ \mathbf{T}\\ \mathbf{N}_1\end{pmatrix}=\begin{pmatrix}\cos\varphi & 0 & \sin\varphi\\ 0 & 1 & 0\\ -\sin\varphi & 0 & \cos\varphi\end{pmatrix}\begin{pmatrix}\mathbf{B}\\ \mathbf{T}\\ \mathbf{N}\end{pmatrix}, \tag{31}$$

where ***N***$_1$ and ***B***$_1$ are the normal vector and binormal vector after twist. Combining Eqs. (30) and (31), the kinematic equation after twist field applied can be derived as:

$$\frac{d}{ds}\begin{pmatrix}\mathbf{B}_1\\ \mathbf{T}\\ \mathbf{N}_1\end{pmatrix}=\boldsymbol{\Lambda}_1\begin{pmatrix}\mathbf{B}_1\\ \mathbf{T}\\ \mathbf{N}_1\end{pmatrix}, \tag{32}$$

$$\boldsymbol{\Lambda}_1=\begin{pmatrix}0 & -\kappa\sin\varphi & \varphi_s-\tau\\ \kappa\sin\varphi & 0 & \kappa\cos\varphi\\ \tau-\varphi_s & -\kappa\cos\varphi & 0\end{pmatrix}. \tag{33}$$

Comparing Eqs. (21) and (33), a set of equations are given to build the bridge between the geometry parameters of target curve $\{\kappa(s), \tau(s)\}$ and the materials properties $\theta(s)$, the principal curvature κ_1 (determined by volume fraction), as well as the twist field $\varphi(s)$:

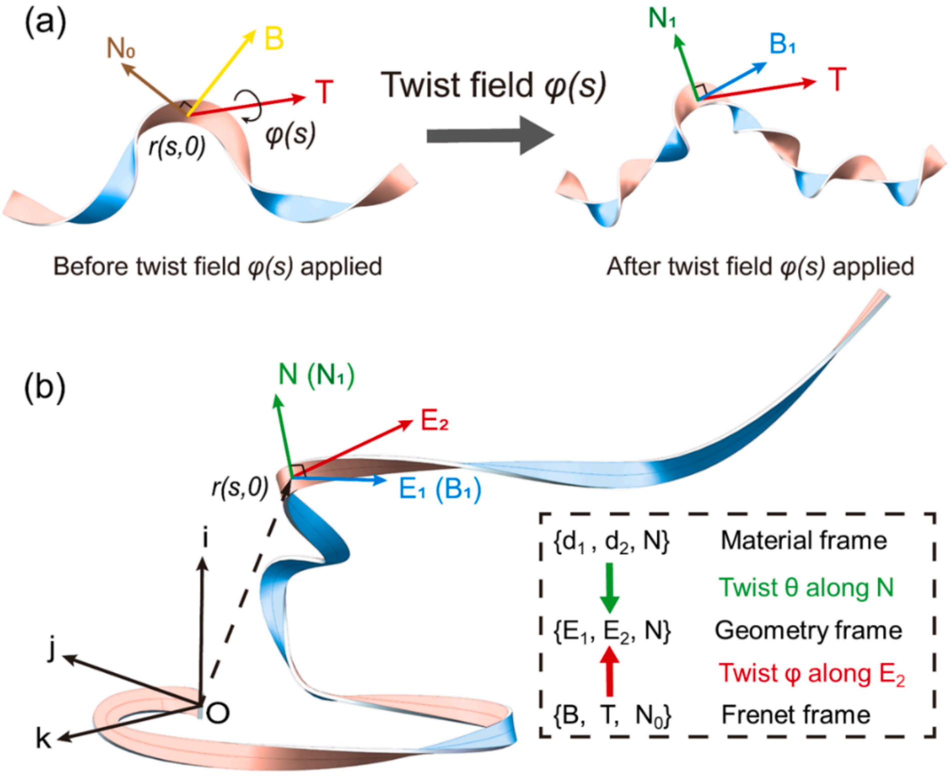

Fig. 5. Schematic illustration of (a) the target space curve before and after twist field applied and (b) the frame transformation of BTM.

$$\begin{cases} \theta' = \kappa \sin\varphi \\ \varphi' = \tau - \kappa \tan 2\theta \cos\varphi \end{cases}, \tag{34}$$

$$\kappa_1 = \frac{\kappa \cos\varphi}{\cos 2\theta}. \tag{35}$$

We note that Eq. (34) is an initial value problem of ordinary differential equations, which can be solved directly with θ_0 and φ_0 as initial values are given. After Eq. (34) is solved, Eq. (35) can be integrated directly and volume fraction $c_m(s)$ can be solved inversely by Eq. (17). Eventually, $c_m(s)$ and $\theta(s)$ as functions of arc length parameter s can be solved for given $\{\kappa(s), \tau(s)\}$ of target curve.

We summarize the multiscale theoretical framework for inverse design in Fig. 5(b). We firstly derive the constitutive of swelling (Eq. (5)) and the principal curvatures of each unit (Eq. (17)). Then the forward problem is solved by rotating the material frame (represent the materials properties) with θ along normal vector $\boldsymbol{N}$ to derive the geometry frame (represents the ribbon morphology) using Eqs. (21) and (22). Eventually, inverse design is achieved by introducing a twist field along the tangent vector to connect the target curve and ribbon morphology (Eqs. (34) and (35)).

3.2. *The optimization of twist field*

As mentioned in Section 3.1, the twist field $\varphi(s)$ for a specific space curve is not unique, as illustrated in Fig. 5(a). Therefore, determining the "best" twist field becomes a critical consideration. Note that for forward problem only the kinematic equation of geometry frame Eq. (20) and (21) needs to be solved, which means when the $\theta(s)$ and $c_m(s)$ are given, the ribbon morphology is unique. However, the solution is not unique for the inverse design problem. We notice that when $\kappa(s)$ and $\tau(s)$ are known, the solution of Eq. (34) is determined by the initial values of θ and φ. Therefore, the initial values of θ and φ are critical for inverse design and we will give a strategy for deriving the appropriate initial conditions of Eq. (34) based on the minimization of errors from discrete units as follows.

Before delving into the selection of initial conditions, we recall that the ribbon is discretized by many units and we approximate the solution of Eqs. (17), (34) and (35) with the c_m and θ discretely in each unit. Therefore, two intuitive problems are necessary to be addressed. Firstly, as illustrated in Fig. 6(a), a significant difference in θ between two adjacent encoding units lead to interfacial mismatch during morphing. Secondly, when dealing with a solution of θ that undergoes drastic changes, a greater number of encoding units are required to discretize it to maintain controlled error, as demonstrated in Fig. 6(b) Case A. Conversely, for solutions of θ that change more gradually, fewer encoding units are necessary, as depicted in Fig. 6(b) Case B. To effectively mitigate the errors resulting from these two issues, we define a loss function U_θ as

$$U_\theta = \int_0^{s_0} \theta'^2 ds. \tag{36}$$

Then, our objective is to determine the suitable boundary conditions $\{\theta(0), \varphi(0)\}$ that minimize the loss function U_θ. Therefore, an optimization problem can be posed as:

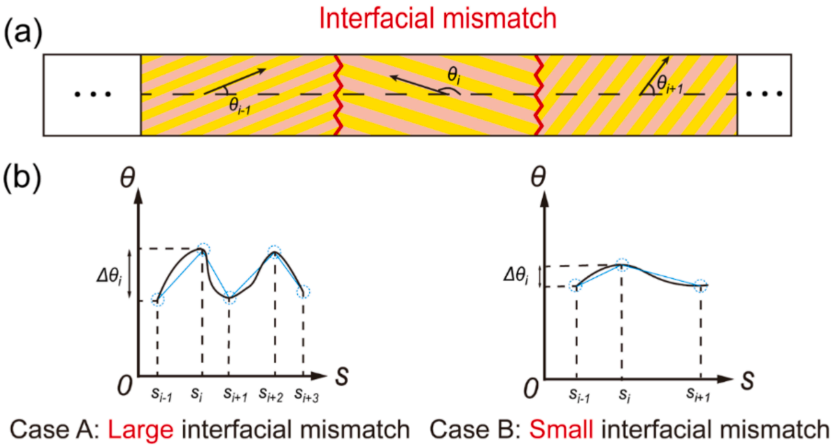

Fig. 6. The optimal design of interfacial mismatch. (a) The schematic illustration of the interfacial mismatch between different units of BTM. (b) Two cases with different relationships of curve and interfacial mismatch. Large and small interfacial mismatch for case A and case B respectively.

$$\begin{aligned}
&\underset{\{\theta_0,\varphi_0\}}{min}\ U_\theta(\theta_0,\varphi_0)=\int_0^{s_0}\theta'^2ds\\
&s.t.\begin{cases}\theta'=\kappa\sin\varphi\\ \varphi'=\tau-\kappa\tan2\theta\cos\varphi\\ \theta(0)=\theta_0\\ \varphi(0)=\varphi_0\end{cases}\\
&\theta_0\in[-\pi/4,\pi/4),\varphi_0\in[-\pi,\pi)
\end{aligned} \tag{37}$$

It is worth noting that there are two alternative kinds of loss functions based on different considerations. The first one is based on the consideration of interfacial mismatch as shown in Eq. (37). However, because of the small swelling strain η as stated in Section 2.2.1 (assumptions (iv)), the principal curvature κ_1 cannot be very large, therefore we can define the second kind of loss function as the integration of $\kappa_1^2+\theta'^2$ as detailed in Appendix C. These two kinds of loss functions give the similar results as shown in the following example (Appendix C and Fig. 11(b)), because the interfacial mismatch is the core factor that determines whether inverse design can be achieved. Thus, here we select the integration of θ'^2 as the loss function.

Before solving the Eq. (37) numerically, we notice that the large twist field of a ribbon leads to the morphology transformation from helicoid to helix and the complex nonlinear mechanical behavior (Armon et al., 2014, 2011; Gomez et al., 2023; Grossman et al., 2016). Therefore, we analyze the stability of Eq. (34) qualitatively to control the increase of $\varphi(s)$. Note that the eigenvalues of Jacobi near the fixed points characterize the stability of ordinary differential equations, when the real parts of the eigenvalues are negative the solution is stable (Datseris and Parlitz, 2022). Without loss of generality, we consider the curvature and torsion of target curve is near zero at the beginning point (arc length parameter $s=0$), because for arbitrary target space curve we can splice a small arc (with small curvature) at the beginning point. Therefore, θ_0 and φ_0 can serve as fixed points of Eq. (34), which leads $\theta^{\grave{}}=\kappa\sin\varphi_0=0$, $\varphi^{\grave{}}=\tau$-$\kappa\tan2\theta_0\cos\varphi_0=0$. To prevent the increase of $\varphi(s)$, we limit the real part of eigenvalues less than zero for θ_0 and φ_0.The Jacobi of Eq. (34) is expressed as:

$$\begin{pmatrix}0 & \kappa\cos\varphi\\ -2\kappa\sec^2 2\theta\cos\varphi & \kappa\sin\varphi\tan2\theta\end{pmatrix}. \tag{38}$$

The eigenvalues of Eq. (38):

$$\begin{cases}\kappa\sec^2 2\theta\sin\theta\cos\theta\cos2\theta\sin\varphi\left(1-\sqrt{1-8\cot^2\varphi\csc^2 2\theta}\right)\\ \kappa\sec^2 2\theta\sin\theta\cos\theta\cos2\theta\sin\varphi\left(1+\sqrt{1-8\cot^2\varphi\csc^2 2\theta}\right)\end{cases}. \tag{39}$$

We should choose the optimal solution to meet that the real part of Eq. (39) is negative to control the increase of twist field. Note that the curvature in Frenet frame is always positive, so the sign of the real part of Eq. (39) is determined by λ_1 and λ_2.

$$\begin{cases}\lambda_1=\sin\theta\cos\theta\cos2\theta\sin\varphi\left(1-\sqrt{1-8\cot^2\varphi\csc^2 2\theta}\right)\\ \lambda_2=\sin\theta\cos\theta\cos2\theta\sin\varphi\left(1+\sqrt{1-8\cot^2\varphi\csc^2 2\theta}\right)\end{cases}. \tag{40}$$

The contour map of the Eq. (40) is shown in Fig. 7. It is obvious that when θ_0 and φ_0 have the opposite signs, the real parts of eigenvalues are negative and the increase of twist field is controlled.

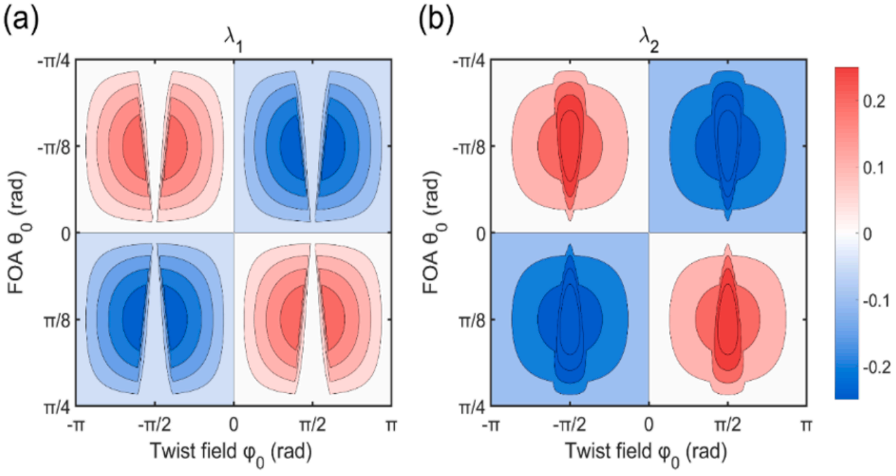

Fig. 7. The contour map of Eq. (40). The color represents the value of eigenvalues, red represents positive and blue represents negative. (a) The reduced first eigenvalue λ_1. (b) The reduced second eigenvalue λ_2.

3.3. The design criteria of geometry size

To give guidelines for the manufacture of BTM experimentally, the design criteria of geometry size, encompassing parameters such as length, width, and thickness, is necessary to control the error. It is crucial to always remember that Eqs. (5) and (17) are only applicable to cases with small strains and small thicknesses. When the strain is significant, the specific geometry boundary of the ribbon will result in the nonlinear relationship between swelling strain and the principal curvature, which brings the difficulties for inverse design (Liu et al., 2023, 2019). The design criteria are also closely intertwined with the specific shape of the target curve. Intuitively, if a target curve exhibits significant curvature, we require more units to encode. Therefore, evaluating the minimal number of units required according to the curvature of target curve is also necessary.

Assume that the maximum bending angle of an unit is $\vartheta_{\max}$ and the local curvature of the unit can be written as $\vartheta_{\max}/l_0$. So combining Eq. (17), we can write:

$$\kappa_2 = f(c_m, \delta, \nu)\frac{\eta}{t} = \frac{\vartheta_{max}}{l_0}, \tag{41}$$

where $f(c_m, \delta, \nu)$ is a dimensionless principal curvature plotted in Fig. 4(a). Hence the length thickness ratio of the unit can be written as:

$$\frac{t}{l_0} = \frac{f(c_m, \delta, \nu)\eta}{\vartheta_{max}}. \tag{42}$$

Linear relationship is only valid when $\eta < 3\%$ (Liu et al., 2019), if we assume the maximum bending angle of an unit is π, the thickness length ratio should be restricted as:

$$\frac{l_0}{t} > \frac{100\pi}{3f(c_m, \delta, \nu)}. \tag{43}$$

We set $\nu = 0.3$, and the result is shown in Fig. 8(a). As the stiffness ratio increases, the anisotropy of the material also increases, resulting in a smaller length-thickness ratio being available. It is important to note that there is a minimum point of the length-thickness ratio for a specific volume fraction. This represents the limitation of the length-thickness ratio under the specific stiffness ratio. If the length thickness ratio is less than this value, the geometry boundary will bring error for morphing morphology.

Similar to the length thickness ratio, the width thickness ratio also influences the morphology of BTM. Consider a special case only with twist field, when θ equals π/4, the morphing shape is helicoid. When the dimensionless width $w/t\sqrt{2\eta f(c_m, \delta, \nu)}$ increases, the helicoid transforms to transforms into helix. It has been investigated by form studies that the critical value of dimensionless width is about 3 (Armon et al., 2014, 2011; Grossman et al., 2016; Hall et al., 2023). To prevent morphological transformation, we have:

$$\frac{w}{t}\sqrt{2\eta f(c_m, \delta, \nu)} < 3. \tag{44}$$

Consequently, width thickness ratio should be restricted as:

$$\frac{w}{t} < \frac{3}{\sqrt{2\eta f(c_m, \delta, \nu)}}. \tag{45}$$

We set $\nu = 0.3$, Eq. (45) is shown in Fig. 8(b). Similar to the length thickness ratio, there is also a minimal point for a specific volume fraction. It means the width thickness ratio should be smaller than this point at least.

We examine a curve, whose length is s_0, and the maximum curvature is κ_m. The actual length of the ribbon in manufactory is L, with

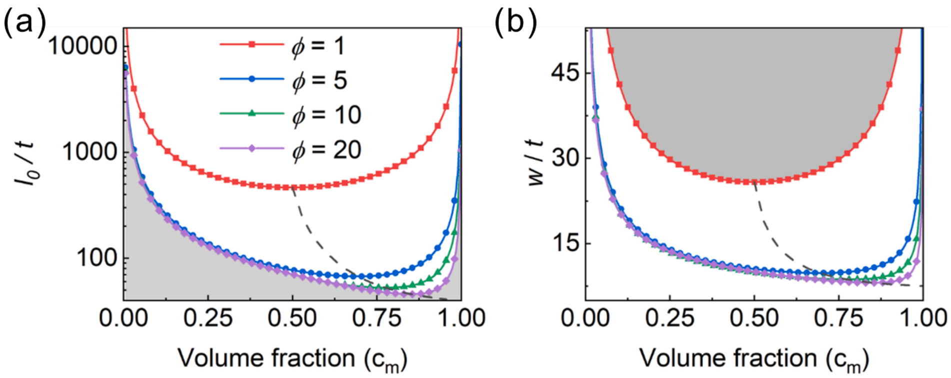

Fig. 8. The design criteria for geometry size. (a) The minimal length-thickness ratio as a function of matrix volume fraction under different fiber-matrix stiffness ratios. (b) The maximal width-thickness ratio as a function of matrix volume fraction under different fiber-matrix stiffness ratios. The dashed line is the minimal point of the length-thickness ratio and width-thickness ratio.

N encoding units. Consequently, the length of each unit is $l_0 = L/N$. To ensure that the maximum curvature of each unit can attain the actual maximum curvature in the target shape of the ribbon $\kappa_m\, s_0/(N\, l_0)$, we have:

$$\kappa_0 = f(c_m, \delta, \nu)\frac{\eta}{t} = \frac{\kappa_m s_0}{N l_0}. \tag{46}$$

The number of units N reads:

$$N = \frac{1}{\eta f(c_m, \delta, \nu)}\frac{t}{l_0}\kappa_m s_0, \tag{47}$$

Eq. (47) shows that for the target curve with larger curvature or longer length, more units are needed to discretize it, which is consistent with our qualitative understanding.

4. Examples and verifications

Based on the multiscale theoretical framework that has been formulated for the inverse design, now we consider some examples to verify our theory. In this section, we consider plane curves, including cardioid and clover at first and further examples, such as curved surfaces with positive and negative Gaussian curvatures discretized by space curve as well as tendril in nature, are designed inversely based on BTM theory. Note that although new methods are developed recently to design the plane curves inversely, such as machine learning (Sun et al., 2024, 2022) and discrete elastic rod (Qin et al., 2022), the inverse design of space curve is still far from being properly investigated. Examples are displayed as follows.

4.1. Examples of plane curves

As shown in Fig. 9(b), the first case is the cardioid, which can be expressed with Eq. (48):

$$x = (1-\cos(2\pi t))\sin(2\pi t), y = (1-\cos(2\pi t))\cos(2\pi t)\, t \in [0, 1). \tag{48}$$

The signed curvature of plane curve is defined as:

$$\kappa = \frac{x'(t)y''(t) - y'(t)x''(t)}{(x'(t)+y'(t))^{3/2}}, \tag{49}$$

where (·)\` donates $d(\cdot)/dt$ and (·)\`\` donates $d^2(\cdot)/dt^2$. By solving Eqs. (34) and (35), we can get the c_m and θ as function of arc length parameter as shown in Fig. 9(a). The curvature at $(x(0), y(0))$ points in infinite, so we just consider $t \in [0.05, 0.95]$. The volume fraction is scaled by the maximum value (0.852) here and in later cases. Then we perform 100 units in FEA as shown in Fig. 9(c), it is obvious that the maximum point of strain has the maximum curvature at $(x(0.05), y(0.05))$ and $(x(0.95), y(0.95))$ and it is almost the same as

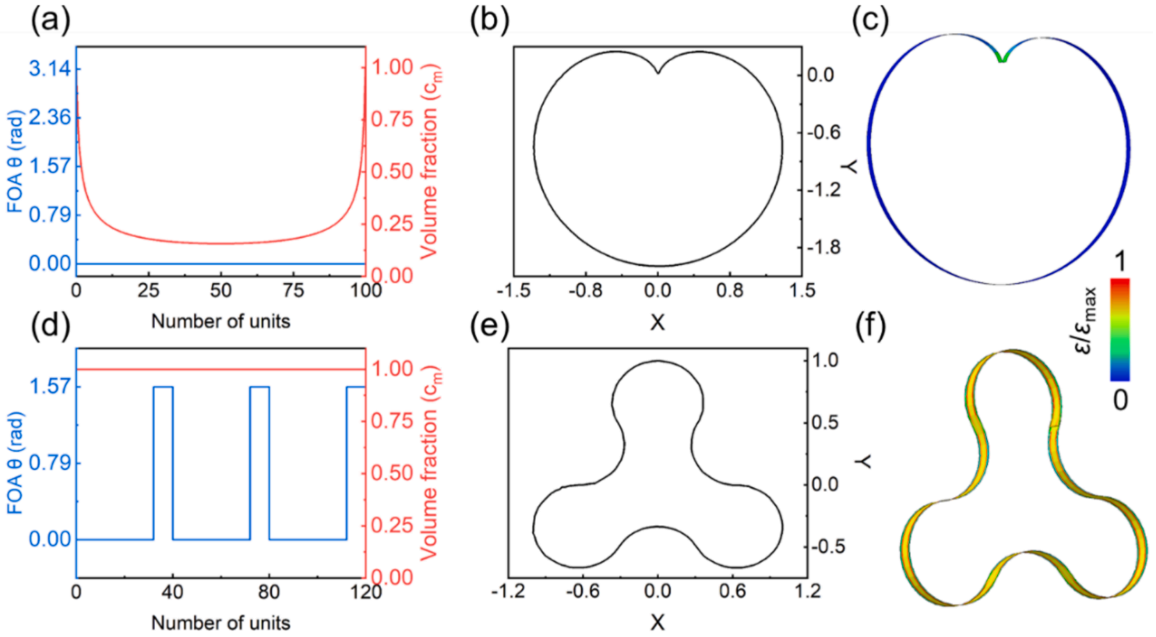

Fig. 9. The inverse design of 2D curves. (a) FOA and volume fraction for cardioid (b) the target cardioid (c) the FEA results of cardioid; (d) the FOA and volume fraction for clover curve (e) the target clover curve (f) the FEA results of clover curve.

the target shape in Fig. 9(b).

As stated in Section 2.2.3, we can morph a plane curve with both positive and negative curvatures by adjusting θ as 0 or π/2. So we choose the second case: the clover curve as shown in Fig. 9(e), which has both the positive and negative curvatures. The c_m and θ is shown in Fig. 9(d). The clover curve is composed of three arcs with 120 degrees center angle and three arcs with 240 degrees center angle, the binormal direction of which are the opposite of the previous ones. Therefore θ has a form similar to square waves. Owing to the same curvature of the six arcs, the volume fraction is the constant. The FEA result shows in Fig. 9(f) verifies our theory.

4.2. Examples of the curve-discretized surfaces

Inverse design of a curved surface morphing from a plane has caused great interests of both experimental and theoretical scientists during past ten years (Aharoni et al., 2018; Boley et al., 2019; Siéfert et al., 2019; Sydney Gladman et al., 2016; van Rees et al., 2017; Yang et al., 2023b). As stated by *Theorema Egregium*, the Gaussian curvature is uniquely determined by the first fundamental form of a surface. Therefore, substantial stretch in plane occurs when morphing from a plate (with zero Gaussian curvature) to a curved surface (with non-zero Gaussian curvature). The substantial stretch poses two significant challenges both in theory and experiments. Generating significant intrinsic strain experimentally to achieve substantial in-plane stretch is indeed challenging using conventional methods like swelling or heating. These methods typically cannot induce enough strain to cause substantial stretch in plane. Inflation, on the other hand, has been used successfully to achieve large in-plane stretches. When rubber materials undergo large strains, they usually exhibit hyper-elastic behavior, which differs significantly from the behavior predicted by linear elastic models. Consequently, a hyper-elastic constitutive model, rather than a linear elastic one, is required to accurately describe the deformation behavior of the material, the formula of which is too complex to guide experiments. Relevant theoretical work has recently been carried out by Ciarletta et al. (Ciarletta et al., 2022). How to achieve inverse design of a curved surface with large Gaussian curvature is still a challenging problem.

By using BTM theory and discretizing the curved surface with space curve, we can morphing the surface with large Gaussian curvature from a plate ribbon (Video S1 and S2). As shown in Fig. 10(c) and (g), two representative curved surfaces, the hyperboloid and hemisphere, with negative and positive Gaussian curvatures are selected. The space curve in Eqs. (50) and (51) are used to discretize the hyperboloid and hemisphere as the objective shown in Fig. 10(c) and (g).

$$\begin{cases} x = \left(6\left(t^2 - t\right) + 3\right)\cos(20\pi t) \\ y = \left(6\left(t^2 - t\right) + 3\right)\sin(20\pi t) \;\; t \in [0, 1) \\ z = 5t \end{cases} \tag{50}$$

$$\begin{cases} x = \cos(30\pi t)\sin(\pi t) \\ y = \sin(30\pi t)\sin(\pi t) \;\; t \in [0.05, 0.5] \\ z = \cos(\pi t) \end{cases} \tag{51}$$

The detail of discretization is shown in Appendix D. Combining Eq. (34), boundary condition $\{\theta_0 = 0,\ \varphi_0 = 0\}$, and the curvature and torsion calculated by Eq. (S14), we can solve the twist field, c_m and θ as shown in Fig. 10(a-b) and (e-f).

It is obvious that in Fig. 10(b), the maximum point of volume fraction is in the middle, which is consistent with the geometric intuition (the curvature is the maximum in the middle of the hyperboloid). FEA results in Fig. 10(d) show that the maximum strain lies on the middle of the hyperboloid, on which the point with maximum curvature lies. This is consistent with the positive correlation between strain and curvature shown in Fig. 10(a-b). For the hemisphere shown in Fig. 10(g), the maximum point of volume fraction lies at the initial points, which is the maximum point of the curvature. Similar FEA result is shown in Fig. 10(h). Note that both for the hyperboloid and hemisphere, we choose the boundary condition $\{\theta_0 = 0,\ \varphi_0 = 0\}$ and the twist field is very small (Fig. 10(a) and (e)). However, when the target space curve is more complex, the twist field is large and the theory in small strain case cannot predict the ribbon shape after morphing. Under this situation, we need to optimize the θ_0 and φ_0 as discussed in Section 3.2. As an instance, a large twist field is needed for inverse design of tendril. In next section, we will design the tendril inversely by optimization.

4.3. Tendril

We illustrate the process of optimal design using the morphology of tendril as an instance shown in Fig. 11(a). The tendril is composed of two parts, the straight line part and the space curve part as shown in the Appendix E. The straight line part is trivial and can be designed by the ribbon without morphing, so we consider the part of the space curve part.

To solve the optimization problem Eq. (37), we scan the initial value θ_0 from -π/4 to π/4 and φ_0 from -π to π and construct the landscape of the loss function Eq. (36) as shown in Fig. 11(b). We selected three solutions for analysis: two with minimal loss values (points 1 and 2) and one with a maximal loss value (point 3) for contrast. As illustrated in Fig. 11(a), the local twist, indicated by the gray circle, is significantly larger than that in the red circle. This suggests that the solution corresponding to point 3 exhibits a pronounced twist, leading to a tendency toward bulking and deviation from the target morphology. To quantitatively assess the optimization results, the corresponding φ, θ, and θ' values for points 1, 2, and 3 as functions of unit number are presented in Fig. 11(c-e). It is evident that the twist field at point 3 increases markedly, reaching a value of 8.0, whereas the twist field at point 1 fluctuates between −0.8 and 0.45 (Fig. 11(c)). Additionally, the θ and θ' values at point 3 are larger than those at points 1 and 2 (Fig. 11(d-e)), indicating that the optimized points 1 and 2 are more stable. This behavior can be explained by the earlier eigenvalue analysis: point 1 is situated

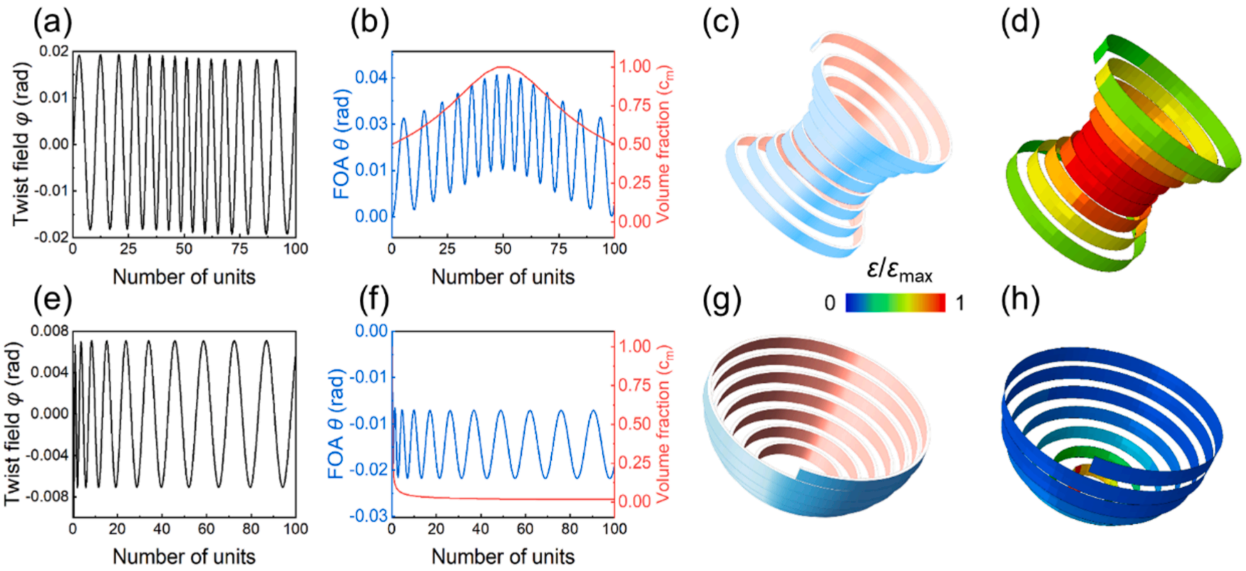

Fig. 10. The inverse design of 3D surface. The twist field, volume fraction and FOA as a function of number of units for the hyperboloid of revolved surface (a-b) and the hemisphere surface (e-f) respectively. The target shape and FEA results for hyperboloid of revolved surface (c-d) and the hemisphere surface (g-h).

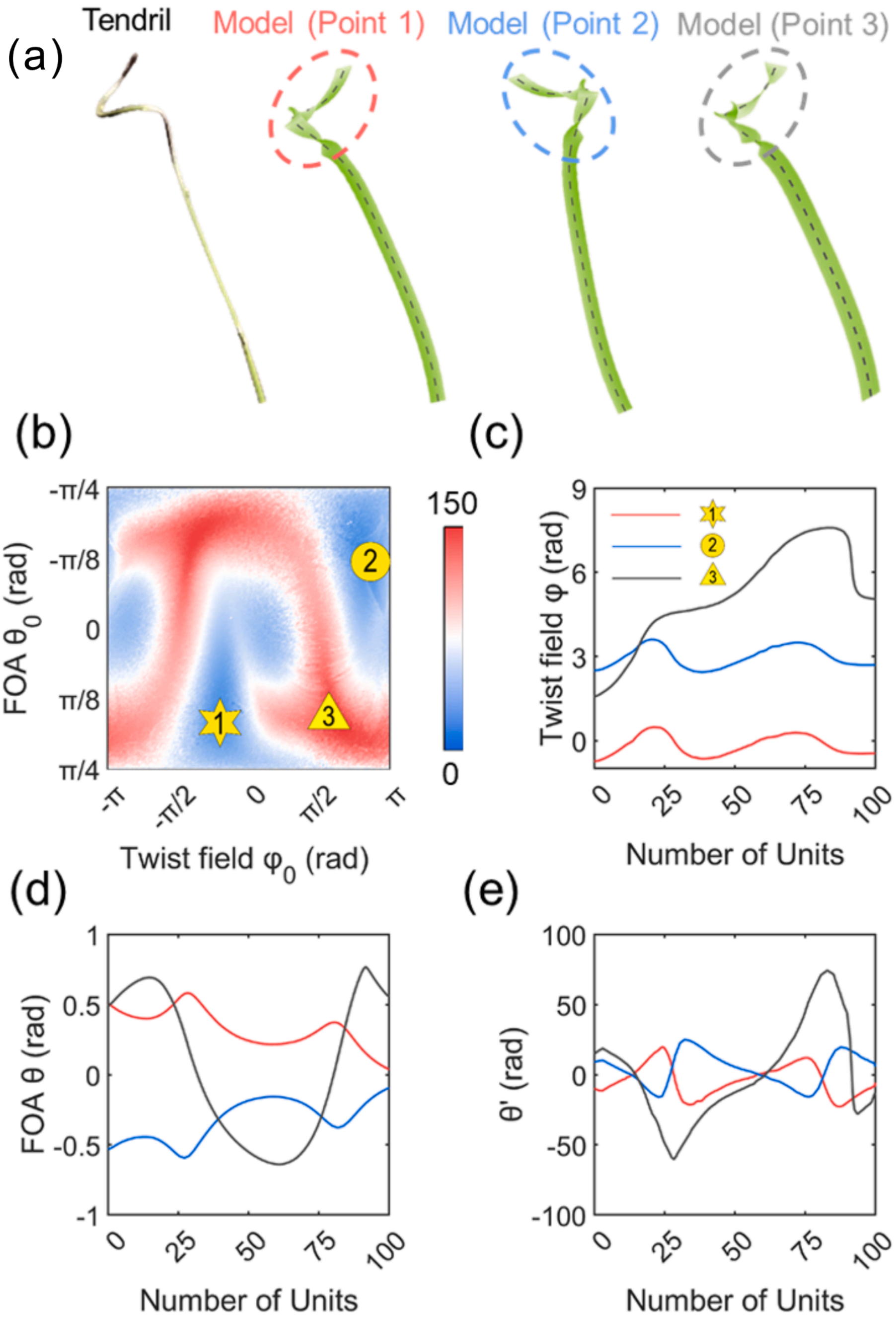

Fig. 11. The inverse design of tendril. (a) The primary tendril and the tendril morphologies inversely solved by BTM theory at point 1(red), point 2 (blue) and point 3(gray). (b) The landscape of integrate value of θ'^2 as loss function versus (θ_0, φ_0), the points 1, 2 are the minimal points and point 3 is the maximal point, respectively. (c-e) The optimal results of twist field, FOA and θ' as functions of number of units at points 1, 2 and 3.

in the negative (blue) region, while point 3 is located in the positive (red) region, as shown in Fig. 7. Although both points 1 and 2 represent minimal loss solutions, it is noteworthy that they exhibit chiral symmetry (Fig. 11(a)), similar to the helix case. Consequently, to achieve the same chirality as observed in natural tendrils (Fig. 11(a)), we select solution point 1 as the optimal choice.

Indeed, only with the solution from point 1 instead of point 3, the ribbon can successfully morph to the target tendril morphology according to FEA results (Video S3). The optimization and FEA results are summarized in Fig. 12. The optimal solution (point 1) is consistent with our geometric intuition: there are two maximal points in Fig. 12(a-b), which correspond to the twice twists of the tendril. To quantify the error of this case, we calculate the error along x, y and z axis in Fig. 12(d) by Eq. (52):

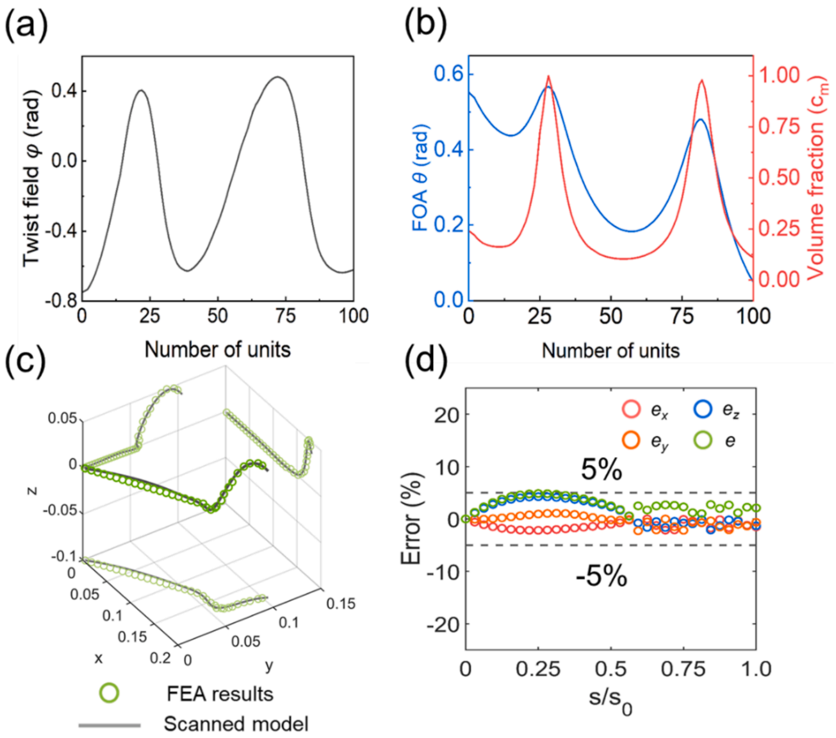

Fig. 12. The optimization and FEA results of tendril. (a-b) The twist field, FOA and c_m as functions of number of units at point 1. (c) The scanned tendril model (gray line) and FEA results (green circle). (d) The error between FEA results and the scanned tendril model.

$$
\begin{aligned}
&e_x = \frac{x_{FEA} - x_{scanned}}{x_{scanned}}; e_y = \frac{y_{FEA} - y_{scanned}}{y_{scanned}} \\
&e_z = \frac{z_{FEA} - z_{scanned}}{z_{scanned}}; e = \sqrt{e_x^2 + e_y^2 + e_z^2}
\end{aligned}
, \tag{52}
$$

where x_{FEA}, y_{FEA}, z_{FEA} are the coordinates in FEA results, $x_{scanned}$, $y_{scanned}$, $z_{scanned}$ are the coordinates in target scanned model and e_x, e_y, e_z, e are the errors along x, y, z axis respectively and the Lˆ2 norm of them. As shown in Fig. 12(d), we control the error within plus or minus 5% by our optimization strategy and the FEA result is coincident with the scanned model (Fig. 12(d)).

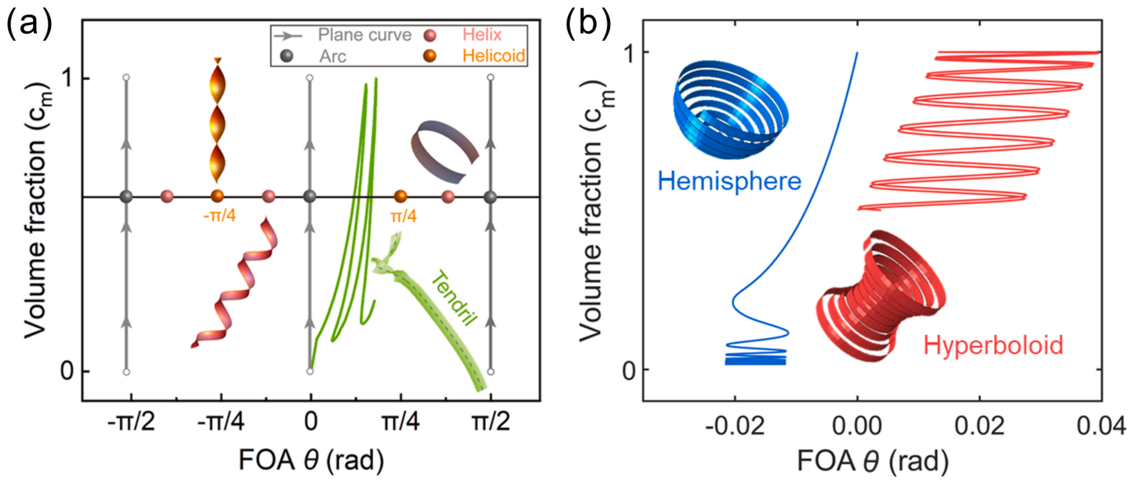

Fig. 13. The phase diagram for morphing ribbon. (a) The phase diagram of previous morphologies and tendril. The gray line represent the gradient curvature for plane curves. The gray, pink and orange points represents the arc, helix and helicoid morphologies, respectively. The green curve represents the inverse design of tendril. (b) The phase diagram for curve-discretized hemisphere surface and hyperboloid of revolved surface. The blue and red lines represent the hemisphere surface and hyperboloid of revolved surface, respectively.

During the optimization, we notice that the initial value of θ is about 0.55, which is near $1/2\arctan(\tau(0)/\kappa(0))$, it a solution of Eq. (24). It means the microstructure of the initial point like helix is near the minimal point. Usually for a general space curve, scanning the full field of θ_0 and φ_0 is expensive for computing resource. Therefore, we can choose a cheaper strategy: minimize the loss function U_θ near $\theta_0 = 0.5\cdot\arctan(\tau(0)/\kappa(0))$ and a random φ_0 or a compromise one: only fix $\theta_0 = 0.5\cdot\arctan(\tau(0)/\kappa(0))$ and scan φ_0 from -π to π. In summary, BTM theory can achieve the inverse design of the target space curves with both curvature and torsion, such as curve-discretized surfaces and creatures with slender structures in nature, effectively.

5. Discussion of the phase diagram for morphing ribbon

Fig. 13 presents a comparison between BTM and previous works, where the morphology of each morphing ribbon is represented as a trajectory in the parametric space of c_m (matrix volume fraction) and θ (fiber orientation angle). To the best of our knowledge, most previous studies on the inverse design of morphing ribbons fall into two categories. The first category consists of plane curves with graded curvature (gray lines in Fig. 13(a)), which can be fabricated with graded stiffness strategy and has been used to design the circumferentially discrete part of the revolved surface (Liu et al., 2020; Sun et al., 2024; Yang et al., 2023a; Zhang, 2022). The second category includes space curves with constant curvature and torsion, such as the arc, helicoid and helix (gray, orange and pink dots in Fig. 13(a)), which can be achieved by using constant c_m and θ (Armon et al., 2011; Chen et al., 2011, 2012; Yue et al., 2023). We notice that the two categories correspond to the two kinds of morphologies of hydration actuated plant tissues as discussed in Section 1. However, BTM theory is not limited to imitate the existing morphologies, but combines the microstructural regulation mechanisms behind them to achieve reverse design of more complex morphologies. In essence, we not only learn from nature, but also transcend nature. As one of the advantages of the BTM theory, we overcome the restriction by *Theorema Egregium* and achieve the morphing of surfaces with large positive and negative Gaussian curvature through discretized curves: hemisphere surface (blue curve in Fig. 13(b)) and hyperboloid of revolved surface (red curve in Fig. 13(b)), which are difficult to be achieved by a morphing plate with relatively low actuation strain. We also imitate the tendril's morphology in nature (green curve in Fig. 13(a)) using BTM. Owing to its capability of designing the curvature and torsion of space curves, BTM is promising to design the metamaterials with more complex 3D shape morphing in the future beyond that of 2D lattice materials (Sun et al., 2024).

Some other perspectives of BTM are stated as follows. Firstly, the length of discrete units in this work is uniform, which is not necessary and may be improved. For example, adaptive unit length may be used for regions with different curvatures, such as using small-length units for large-curvature part and large-length units for small-curvature part, which would make the fabrication easier. Such non-uniform design strategies will be further investigated. Secondly, when the ribbon has magnetic, electrical or optical properties, BTM has potential to regulate the physical field by the target geometric morphology, which is more promising compared with traditional strain engineering (B. Li et al., 2024; J. Li et al., 2024; Yang et al., 2024; Zhu et al., 2015). Lastly, not only limited to the residual strain by external stimuli, Eqs. (34) and (35) are the general principle for inverse design of target space curve and they can be used in many other fields such as the geometric design of the robotic gripper with tendon actuated, architectural structures (Lee and Xie, 2020; Siéfert, 2019; Siéfert et al., 2020) and flexible electronics assembly (Xu et al., 2015).

6. Conclusion

In summary, a multiscale theoretical framework named BTM is proposed to realize the inverse design of space curves with both curvature and torsion, beyond the previous design strategies of morphologies of morphing ribbons (arc, helix helicoid and plane curve). The BTM and associated theory are inspired from two microstructural deformation mechanisms in natural plants: the graded curvature regulated by matrix c_m and the helix-like morphology regulated by FOA. To solve the c_m and FOA inversely, we innovatively introduce a twist field to convert the forward problem of morphing ribbon into an inverse problem. At last, as a conceptual display, we present a phase diagram in the c_m versus FOA plane to compare the complex target morphologies (e.g., hemisphere, hyperboloid, and tendril), characterized by various curvatures and torsions designed by the BTM theory.

In the BTM theoretical framework, a multiscale swelling constitutive is proposed in material frame to describe the swelling strains, and the principal curvatures of each unit are derived in material frame by minimizing the elastic energy. Then, the rotation θ along the normal vector $\boldsymbol{N}$ is applied to connect the material frame and the geometry frame. Furthermore, a twist field φ is introduced to achieve the inverse design, which builds the bridge between material properties (in material frame) and the geometry of target space curve (in Frenet frame). Considering the fact that the solution for inverse design is not unique, we provide an optimization strategy for the twist field selection. The design criteria of geometry size are also provided based on the consideration of fabrication, and some cases are selected to verify the theory by FEA. Therefore, the BTM theory paves the way for the inverse design and intelligent fabrication of morphing ribbons, and is thus promising in facilitating broader applications of morphing materials.

CRediT authorship contribution statement

JiaHao Li: Writing – original draft, Software, Methodology, Investigation, Data curation. **Xiaohao Sun:** Writing – original draft, Methodology, Formal analysis. **ZeZhou He:** Methodology. **YuanZhen Hou:** Methodology. **HengAn Wu:** Writing – review & editing, Validation, Supervision, Resources, Project administration, Funding acquisition. **YinBo Zhu:** Writing – review & editing, Writing – original draft, Validation, Supervision, Resources, Funding acquisition, Formal analysis, Conceptualization.

Declaration of competing interest

The authors declare that they have no known competing financial interests or personal relationships that could have appeared to influence the work reported in this paper.

Acknowledgments

We thank Prof. Haiyi Liang and Prof. Linghui He at University of Science and Technology of China for helpful discussions. This work was jointly supported by the Youth Innovation Promotion Association CAS (2022465), the National Natural Science Foundation of China (12232016, 12172346, and 12202431), the USTC Tang Scholar, the Natural Science Foundation of Anhui Province (2208085QA24), the Postdoctoral Fellowship Program of CPSF (GZB20240712), and China Postdoctoral Science Foundation (2024M763149). The numerical calculations have been done on the supercomputing system in Hefei Advanced Computing Center and the Supercomputing Center of University of Science and Technology of China.

Supplementary materials

Supplementary material associated with this article can be found, in the online version, at doi:10.1016/j.jmps.2024.105999.

Data availability

Data will be made available on request.

References

Abbena, E., Salamon, S., Gray, A., 2006. Modern differential geometry of curves and surfaces with mathematica, Third Edition. CRC Press.
Aharoni, H., Xia, Y., Zhang, X., Kamien, R.D., Yang, S., 2018. Universal inverse design of surfaces with thin nematic elastomer sheets. Proc. Natl. Acad. Sci. U.S.A. 115, 7206–7211.
Armon, S., Aharoni, H., Moshe, M., Sharon, E., 2014. Shape selection in chiral ribbons: from seed pods to supramolecular assemblies. Soft. Matter. 10, 2733–2740.
Armon, S., Efrati, E., Kupferman, R., Sharon, E., 2011. Geometry and mechanics in the opening of chiral seed pods. Science 333, 1726–1730.
Bishop, R.L., 1975. There is more than one way to frame a curve. Am. Math. Mon. 82, 246–251.
Boley, J.W., Van Rees, W.M., Lissandrello, C., Horenstein, M.N., Truby, R.L., Kotikian, A., Lewis, J.A., Mahadevan, L., 2019. Shape-shifting structured lattices via multimaterial 4D printing. Proc. Natl. Acad. Sci. U.S.A. 116, 20856–20862.
Chen, Z., Guo, Q., Majidi, C., Chen, W., Srolovitz, D.J., Haataja, M.P., 2012. Nonlinear geometric effects in mechanical bistable morphing structures. Phys. Rev. Lett. 109, 114302.
Chen, Z., Majidi, C., Srolovitz, D.J., Haataja, M., 2011. Tunable helical ribbons. Appl. Phys. Lett. 98, 011906.
Cheng, X., Fan, Z., Yao, S., Jin, T., Lv, Z., Lan, Y., Bo, R., Chen, Y., Zhang, F., Shen, Z., Wan, H., Huang, Y., Zhang, Y., 2023. Programming 3D curved mesosurfaces using microlattice designs. Science 379, 1225–1232.
Ciarletta, P., Pozzi, G., Riccobelli, D., 2022. The Föppl–von Kármán equations of elastic plates with initial stress. R. Soc. Open Sci. 9, 220421.
Colorado-Cervantes, I., Varano, V., Teresi, L., 2022. Stress-free morphing by means of compatible distortions. Phys. Rev. E 106, 015003.
Cosgrove, D.J., 2024. Structure and growth of plant cell walls. Nat. Rev. Mol. Cell. Biol. 25, 340–358.
Datseris, G., Parlitz, U., 2022. Nonlinear dynamics—a concise introduction interlaced with code. Springer, 2022.
Efrati, E., Sharon, E., Kupferman, R., 2009. Elastic theory of unconstrained non-Euclidean plates. J. Mech. Phys. Solids 57, 762–775.
Gomez, M., Reis, P.M., Audoly, B., 2023. Twisting instabilities in elastic ribbons with inhomogeneous pre-stress: a macroscopic analog of thermodynamic phase transition. J. Mech. Phys. Solids 181, 105420.
Grossman, D., Sharon, E., Diamant, H., 2016. Elasticity and fluctuations of frustrated nanoribbons. Phys. Rev. Lett. 116, 258105.
Ha, J., Choi, S.M., Shin, B., Lee, M., Jung, W., Kim, H.-Y., 2020. Hygroresponsive coiling of seed awns and soft actuators. Extreme Mech. Lett. 38, 100746.
Hall, D.M., Stevens, M.J., Grason, G.M., 2023. Building blocks of non-Euclidean ribbons: size-controlled self-assembly via discrete frustrated particles. Soft Matter 19, 858–881.
Hou, Y., Guan, Q.-F., Xia, J., Ling, Z.-C., He, Z., Han, Z.-M., Yang, H.-B., Gu, P., Zhu, Y., Yu, S.-H., Wu, H., 2021. Strengthening and toughening hierarchical nanocellulose via humidity-mediated interface. ACS Nano 15, 1310–1320.
Huang, C., Wang, Z., Quinn, D., Suresh, S., Hsia, K.J., 2018. Differential growth and shape formation in plant organs. Proc. Natl. Acad. Sci. U.S.A. 115, 12359–12364.
Kansara, H., Liu, M., He, Y., Tan, W., 2023. Inverse design and additive manufacturing of shape-morphing structures based on functionally graded composites. J. Mech. Phys. Solids 180, 105382.
Klein, Y., Efrati, E., Sharon, E., 2007. Shaping of elastic sheets by prescription of non-Euclidean metrics. Science 315, 1116–1120.
Kuang, Y., Chen, C., Cheng, J., Pastel, G., Li, Tian, Song, J., Jiang, F., Li, Y., Zhang, Y., Jang, S.-H., Chen, G., Li, Teng, Hu, L., 2019. Selectively aligned cellulose nanofibers towards high-performance soft actuators. Extreme Mech. Lett. 29, 100463.
Lee, T.-U., Xie, Y.M., 2020. From ruled surfaces to elastica-ruled surfaces: new possibilities for creating architectural forms. In: Proceedings of IASS Annual Symposia 2020, pp. 1–12.
Li, B., Li, J., Jiang, W., Wang, Y., Wang, D., Song, L., Zhu, Y., Wu, H., Wang, G., Zhang, Z., 2024. Anisotropic fracture of two-dimensional Ta2NiSe5. Nano Lett 24, 6344–6352.
Li, J., Hou, Y., He, Z., Wu, H., Zhu, Y., 2024. Strain engineering of ion-Coordinated nanochannels in nanocellulose. Nano Lett 24, 6262–6268.
Liu, M., Domino, L., Vella, D., 2020. Tapered elasticæ as a route for axisymmetric morphing structures. Soft Matter 16, 7739–7750.
Liu, Y., Cao, Y., Feng, X.-Q., Cao, C., 2019. Phase transition and optimal actuation of active bilayer structures. Extreme Mech. Lett. 29, 100467.
Liu, Y., Fu, X., Yang, R., Liu, J., Tee, B.C.K., Liu, Z., 2023. Size-dependent bending of a rectangular polymer film. Soft Matter 19, 4954–4963.
Luo, D., Maheshwari, A., Danielescu, A., Li, J., Yang, Y., Tao, Y., Sun, L., Patel, D.K., Wang, G., Yang, S., Zhang, T., Yao, L., 2023. Autonomous self-burying seed carriers for aerial seeding. Nature 614, 463–470.
Pezzulla, M., Smith, G.P., Nardinocchi, P., Holmes, D.P., 2016. Geometry and mechanics of thin growing bilayers. Soft Matter 12, 4435–4442.
Pezzulla, M., Stoop, N., Jiang, X., Holmes, D.P., 2017. Curvature-driven morphing of non-Euclidean shells. Proc. R. Soc. A. 473, 20170087.

Qin, L., Zhu, J., Huang, W., 2022. A bottom-up optimization method for inverse design of two-dimensional clamped-free elastic rods. Int. J. Numer. Methods. Eng. 123, 2556–2572.

Quan, H., Kisailus, D., Meyers, M.A., 2020. Hydration-induced reversible deformation of biological materials. Nat. Rev. Mater. 6, 264–283.

Rafsanjani, A., Brulé, V., Western, T.L., Pasini, D., 2015. Hydro-responsive curling of the resurrection plant selaginella lepidophylla. Sci. Rep. 5, 8064.

Reyssat, E., Mahadevan, L., 2009. Hygromorphs: from pine cones to biomimetic bilayers. J. R. Soc. Interface. 6, 951–957.

Salmen, L., 2022. On the organization of hemicelluloses in the wood cell wall. Cellulose 29, 1349–1355.

Salmen, L., 2015. Wood morphology and properties from molecular perspectives. Ann. For. Sci. 72, 679–684.

Shin, B., Ha, J., Lee, M., Park, K., Park, G.H., Choi, T.H., Cho, K.-J., Kim, H.-Y., 2018. Hygrobot: a self-locomotive ratcheted actuator powered by environmental humidity. Sci. Robot. 3, eaar2629.

Shen, Z., Hu, X., Tang, Z., Xiao, Y., Wang, S., Cheng, X., Zhang, Y., 2024. Curvature programming of freestanding 3D mesostructures and flexible electronics based on bilayer ribbon networks. J. Mech. Phys. Solids. 191, 105766.

Siéfert, E., 2019. Inflating to shape: from soft architectured elastomers to patterned fabric sheets (phdthesis). Sorbonne Université.

Siéfert, E., Reyssat, E., Bico, J., Roman, B., 2020. Programming stiff inflatable shells from planar patterned fabrics. Soft Matter 16, 7898–7903.

Siéfert, E., Reyssat, E., Bico, J., Roman, B., 2019. Bio-inspired pneumatic shape-morphing elastomers. Nat. Mater. 18, 24–28.

Sun, X., Yu, L., Yue, L., Zhou, K., Demoly, F., Zhao, R.R., Qi, H.J., 2024. Machine learning and sequential subdomain optimization for ultrafast inverse design of 4D-printed active composite structures. J. Mech. Phys. Solids. 186, 105561.

Sun, X., Yue, L., Yu, L., Shao, H., Peng, X., Zhou, K., Demoly, F., Zhao, R., Qi, H.J., 2022. Machine learning-evolutionary algorithm enabled design for 4D-Printed active composite structures. Adv. Funct. Mater. 32, 2109805.

Sydney Gladman, A., Matsumoto, E.A., Nuzzo, R.G., Mahadevan, L., Lewis, J.A., 2016. Biomimetic 4D printing. Nat. Mater. 15, 413–418.

Tao, Y., Lee, Y.-C., Liu, H., Zhang, X., Cui, J., Mondoa, C., Babaei, M., Santillan, J., Wang, G., Luo, D., Liu, D., Yang, H., Do, Y., Sun, L., Wang, W., Zhang, T., Yao, L., 2021. Morphing pasta and beyond. Sci. Adv. 7, eabf4098.

Timoshenko, S., 1925. Analysis of Bi-Metal Thermostats. J. Opt. Soc. Am. 11, 233.

Turing, A.M., 1937. On Computable Numbers, with an application to the entscheidungsproblem. Proc. Lond. Math. Soc. s2-42, 230–265.

Van Rees, W.M., Vouga, E., Mahadevan, L., 2017. Growth patterns for shape-shifting elastic bilayers. Proc. Natl. Acad. Sci. U.S.A. 114, 11597–11602.

Xiao, J.-H., Zhang, Z.-B., Li, J., Chen, S.-M., Gao, H.-L., Liao, Y., Chen, L., Wang, Z., Lu, Y., Hou, Y., Wu, H., Zou, D., Yu, S.-H., 2024. Bioinspired polysaccharide-based nanocomposite membranes with robust wet mechanical properties for guided bone regeneration. Natl. Sci. Rev. 11, nwad333.

Xu, S., Yan, Z., Jang, K.-I., Huang, W., Fu, H., Kim, J., Wei, Z., Flavin, M., McCracken, J., Wang, R., Badea, A., Liu, Y., Xiao, D., Zhou, G., Lee, J., Chung, H.U., Cheng, H., Ren, W., Banks, A., Li, X., Paik, U., Nuzzo, R.G., Huang, Y., Zhang, Y., Rogers, J.A., 2015. Assembly of micro/nanomaterials into complex, three-dimensional architectures by compressive buckling. Science 347, 154–159.

Yang, L., Yue, S., Tao, Y., Qiao, S., Li, H., Dai, Z., Song, B., Chen, Y., Du, J., Li, D., Gao, P., 2024. Suppressed thermal transport in silicon nanoribbons by inhomogeneous strain. Nature 629, 1021–1026.

Yang, X., Liu, M., Zhang, B., Wang, Z., Chen, T., Zhou, Y., Chen, Y., Hsia, K.J., Wang, Y., 2023a. Hierarchical tessellation enables programmable morphing matter. Matter 7, 603–619.

Yang, X., Zhou, Y., Zhao, H., Huang, W., Wang, Y., Hsia, K.J., Liu, M., 2023b. Morphing matter: from mechanical principles to robotic applications. Soft Sci 3, 38.

Yavari, A., 2010. A geometric theory of growth mechanics. J. Nonlinear Sci. 20, 781–830.

Yue, L., Sun, X., Yu, L., Li, M., Montgomery, S.M., Song, Y., Nomura, T., Tanaka, M., Qi, H.J., 2023. Cold-programmed shape-morphing structures based on grayscale digital light processing 4D printing. Nat. Commun. 14, 5519.

Zhang, C., Chen, M., Keten, S., Coasne, B., Derome, D., Carmeliet, J., 2021. Hygromechanical mechanisms of wood cell wall revealed by molecular modeling and mixture rule analysis. Sci. Adv. 7, eabi8919.

Zhang, D., Liu, L., Xu, P., Zhao, Y., Li, Q., Lan, X., Zhang, F., Wang, L., Wan, X., Zou, X., Zeng, C., Xin, X., Dai, W., Li, Y., He, Y., Liu, Y., Leng, J., 2022. World's first application of a self-deployable mechanism based on shape memory polymer composites in Mars explorations: ground-based validation and on-Mars qualification. Smart Mater. Struct. 31, 115008.

Zhang, F., Yang, M., Xu, X., Liu, X., Liu, H., Jiang, L., Wang, S., 2022. Unperceivable motion mimicking hygroscopic geometric reshaping of pine cones. Nat. Mater. 21, 1357–1365.

Zhang, Y., Yang, J., Liu, M., Vella, D., 2022. Shape-morphing structures based on perforated kirigami. Extreme Mech. Lett. 56, 101857.

Zhu, S., Stroscio, J.A., Li, T., 2015. Programmable extreme pseudomagnetic fields in graphene by a uniaxial stretch. Phys. Rev. Lett. 115, 245501.